

HELSINKI INSTITUTE OF PHYSICS

INTERNAL REPORT SERIES

HIP-2006-04

**CHARACTERIZATION OF CZOCHRALSKI  
SILICON DETECTORS**

Panja-Riina Luukka

Helsinki Institute of Physics

P.O. Box 64, FIN-00014 University of Helsinki, Finland

*Dissertation for the degree of Doctor of Science in Technology to be presented with due permission of the Department of Electrical and Communications Engineering for public examination and debate in Micronova large lecture hall at Helsinki University of Technology (Espoo, Finland) on the 26<sup>th</sup> of May, 2006, at 12 o'clock noon.*

Helsinki 2006

ISBN 952-10-2955-2  
ISSN 1455-0563  
Helsinki 2006  
Yliopistopaino

## Acknowledgements

The research for this thesis was carried out during the years 2002-2005 as a member of Helsinki Institute of Physics CMS Tracker project. Most of the work was done at CERN, European Organization for Nuclear Research, but significant amount of tasks were performed in collaboration with the Microelectronics Centre of Helsinki University of Technology and Jyväskylä University Accelerator Laboratory. In addition to electrical characterizations conducted at CERN Solid State Detector Laboratory, some of the measurements were done in Brookhaven National Laboratory, Ioffe Institute, and University of Karlsruhe. I am most grateful to all of these institutions.

I wish to express my warm thanks to Professor Pekka Kuivalainen for supervising my post-graduate studies. I am grateful to the pre-examiners Dr. Mikko Laakso and Dr. Simo Eränen for their kind comments and suggestions to improve the manuscript.

I am particularly grateful to Professor Jorma Tuominiemi for giving me the opportunity to work in the Helsinki Institute of Physics CMS Tracker Project and for his encouragement and confidence in my work. I would like to thank my project leader Dr. Eija Tuominen for the support, encouragement and help during these years. I am indebted to my instructor Dr. Jaakko Härkönen for the professional guidance, tutoring and inspiration throughout the thesis project.

A great number of researchers, whose names are acknowledged in the papers that are part of this thesis, were involved in this work. I wish to express my gratitude to all of them. Especially I would like to thank Esa Tuovinen for processing the samples and Lauri Wendland for the work in H2.

I would like to express my gratitude to all of my friends for the support and friendship.

Finally, I thank my parents Hannu and Marja-Riitta and my godparents Marjut and Yrjö for their continuous support and encouragement during the thesis work and my whole life.

Kumpula, April 4<sup>th</sup>, 2006

Panja Luukka

## Abstract

This thesis describes the characterization of irradiated and non-irradiated segmented detectors made of high-resistivity ( $>1 \text{ k}\Omega\text{cm}$ ) magnetic Czochralski (MCZ) silicon. It is shown that the radiation hardness (RH) of the protons of these detectors is higher than that of devices made of traditional materials such as Float Zone (FZ) silicon or Diffusion Oxygenated Float Zone (DOFZ) silicon due to the presence of intrinsic oxygen ( $> 5 \times 10^{17} \text{ cm}^{-3}$ ). The MCZ devices therefore present an interesting alternative for future high-energy physics experiments. In the large hadron collider (LHC), the RH of the detectors is a critical issue due to the high luminosity ( $10^{34} \text{ cm}^{-2}\text{s}^{-1}$ ) corresponding to the expected total fluencies of fast hadrons above  $10^{15} \text{ cm}^{-2}$ . This RH improvement is important since radiation damage in the detector bulk material reduces the detector performance and because some of the devices produced from standard detector-grade silicon, e.g. FZ silicon with negligible oxygen concentration, might not survive the planned operational period of the LHC experiments.

In this work, segmented detectors and test structures were processed, measured, irradiated with different particles (protons of different energies, neutrons and high-energy electrons) and tested with a  $^{60}\text{Co}$  gamma source and with high-energy muon and pion beams. The electrical characterizations show that, for proton irradiation, the MCZ silicon is significantly radiation harder than traditionally used detector materials. In gamma irradiation, MCZ silicon detectors behave similarly to the DOFZ silicon detectors. For neutron radiation, there is only a small difference between MCZ silicon and the reference devices made of standard FZ silicon. The beam test results with the full-size detectors show that the properties of the high-resistivity MCZ silicon are suitable for particle detection both before and after heavy proton irradiation.

## List of Publications

- I. E. Tuominen, K. Banzuzi, S. Czellar, A. Heikkinen, J. Härkönen, P. Johansson, V. Karimäki, P. Luukka, P. Mehtälä, J. Niku, S. Nummela, J. Nysten, J. Simpura, E. Tuovinen, J. Tuominiemi, D. Ungaro, T. Vaarala, L. Wendland, M. Voutilainen and A. Zibellini, *Test beam results of a large area strip detector made on high resistivity Czochralski silicon*, Nuclear Physics B (Proc. Suppl.) 125 (2003) 175-178.
- II. P. Luukka, J. Härkönen, E. Tuovinen, E. Tuominen, K. Lassila-Perini, P. Mehtälä, S. Nummela, J. Nysten, D. Ungaro, A. Zibellini, P. Laitinen, I. Riihimäki, A. Virtanen, A. Furgeri and F. Hartmann, *Results of proton irradiations of large area strip detectors made on high-resistivity Czochralski silicon*, Nuclear Instruments and Methods in Physics Research A 530 (2004) 117-121.
- III. P. Luukka on behalf of the CERN RD50 Collaboration, *Status of defect engineering activity of the RD50 collaboration*, Nuclear Instruments and Methods in Physics Research A 530 (2004) 152-157.
- IV. P. Luukka, T. Lampén, L.A. Wendland, S. Czellar, E. Hæggström, J. Härkönen, V. Karimäki, I. Kassamakov, T. Mäenpää, J. Tuominiemi and E. Tuovinen, *Test Beam Results of a Proton Irradiated Czochralski Silicon Strip Detector*, Nuclear Instruments and Methods in Physics Research A, accepted for publication.
- V. Z. Li, J. Harkonen, W. Chen, J. Kierstead, P. Luukka, E. Tuominen, E. Tuovinen, E. Verbitskaya and V. Eremin, *Radiation Hardness of High Resistivity Magnetic Czochralski Silicon Detectors After Gamma, Neutron and Proton Radiations*, IEEE Transactions on Nuclear Science 51 (4) (2004) 1901-1908.
- VI. J. Härkönen, E. Tuovinen, P. Luukka, E. Tuominen, Z. Li, A. Ivanov, E. Verbitskaya, V. Eremin, A. Pirojenko, I. Riihimäki and A. Virtanen, *Particle detectors made of high-resistivity Czochralski silicon*, Nuclear Instruments and Methods in Physics Research A 541 (2005) 202-207.

## Author's Contribution

The research has been carried out at the Helsinki Institute of Physics within the CMS Tracker group and in the framework of RD50 Collaboration during the years 2002-2005. The author has participated actively in the electrical characterizations, irradiations and beam tests presented in this thesis and, to a much lesser extent, to the device processing. The publications in this thesis are a result of group effort. The author is the main writer of Publications II, III and IV and has contributed to the other publications (I, IV and VI). The results have also been presented at international conferences.

## **Summary of Publications**

### *I. Test beam results of a large area strip detector made on high resistivity Czochralski silicon*

This paper presents the first beam test results of a full-size (32.5 cm<sup>2</sup>) strip detector processed on n-type magnetic Czochralski silicon. Prior to the beam test, the electrical properties of the detector were found to be appropriate, the detector depleted with a reasonable operating voltage (420 V) with a leakage current of 2.4 μA. Using the Helsinki Silicon Beam telescope, the performance of the Czochralski detector was found to be comparable with detectors made from standard silicon materials. The particle detection efficiency of the device was 95% and the signal-to-noise ratio approximately 10.

### *II. Results of proton irradiations of large area strip detectors made on high-resistivity Czochralski silicon*

This paper describes the measurements performed on test diodes and strip detectors made of Czochralski silicon that were irradiated with 10 MeV protons. The 1 MeV neutron equivalent irradiation doses were  $1.6 \times 10^{14}$  and  $8.5 \times 10^{13}$  cm<sup>-2</sup> for the detectors and up to  $5.0 \times 10^{14}$  cm<sup>-2</sup> for the test diodes. After the irradiation, the depletion voltages and the leakage currents were measured. Czochralski silicon devices proved to be significantly more radiation hard than the reference devices processed on traditional detector materials. For example, the leakage current of the Czochralski silicon devices does not increase linearly as a function of the irradiation dose, as is the case with the standard Float Zone silicon devices. In addition, the Czochralski silicon has the space charge type inversion only after about  $1.6 \times 10^{14}$  1 MeV neutrons cm<sup>-2</sup>.

### *III. Status of defect engineering activity of the RD50 collaboration*

This paper presents the status of defect engineering activity of CERN RD50 Collaboration, the objective of which is to improve the radiation tolerance of the semiconductor sensors used in high-energy physics experiments. The research lines of the collaboration cover a large variety of studies on radiation hardness and radiation effects, including defect modeling, defect characterization, defect engineering, characterization of microscopic effects, new materials and full-size semiconductor detectors. This paper describes the latest experimental results of the defect-engineered detectors.

### *IV. Test Beam Results of a Proton Irradiated Czochralski Silicon Strip Detector*

This paper describes the test beam results obtained with a 32.5 cm<sup>2</sup> microstrip detector processed on n-type magnetic Czochralski silicon. The detector was irradiated with 10 MeV protons to  $1.6 \times 10^{14}$  cm<sup>-2</sup> 1 MeV neutron equivalent fluence. The results show that

the detector was still operational after the received dose and one year of annealing at room temperature. An average signal-to-noise ratio of 3, a spatial resolution of 20  $\mu\text{m}$  and a particle detection efficiency of 36 % were measured.

#### V. *Radiation Hardness of High Resistivity Magnetic Czochralski Silicon Detectors After Gamma, Neutron and Proton Radiations*

This paper presents studies on pad detectors that were fabricated of high-resistivity magnetic Czochralski material and irradiated with  $^{60}\text{Co}$  gamma rays, neutrons and protons to various fluencies with the control detectors made of standard float zone silicon. For gamma radiation, magnetic Czochralski silicon detectors behave similarly to the high-temperature long-time (HTLT) oxygenated float zone silicon detectors, i.e. there is no space charge inversion and there is a build up of positive space charges. For neutron irradiation, there is little difference between the Czochralski and the control sensors; the space charge inversion is observed for both materials. For proton irradiation, the space charge sign inversion fluence for Czochralski detectors is about three times higher than that of Czochralski sensors irradiated with neutrons. Thus, high-resistivity magnetic Czochralski silicon behaves in a manner similar to that of HTLT oxygenated float zone silicon, and is even more radiation hard to the charged particles than the HTLT oxygenated float zone silicon.

#### VI. *Particle detectors made of high-resistivity Czochralski silicon*

This paper describes the radiation hardness properties of magnetic Czochralski silicon detectors irradiated with low- and high-energy protons, neutrons, gamma rays, lithium ions and electrons. Many investigations in the framework of CERN RD50 Collaboration have indicated that Czochralski silicon is more radiation hard than standard and oxygenated Float Zone silicon when subjected to hadron irradiation. An interesting feature of this material is the formation of thermal donors (TD) at certain temperatures. However, with correct processing, the harmful TD generation can be suppressed.

# Contents

Acknowledgements.....	iii
Abstract.....	iv
List of Publications.....	v
Author's Contribution.....	v
Summary of Publications.....	vi
Contents.....	viii
1. Introduction.....	1
2. Theory.....	3
2.1 Silicon growth techniques.....	3
2.1.1 Float Zone silicon.....	3
2.1.2 Czochralski silicon.....	4
2.2 Silicon detectors.....	5
2.2.1 P-n junction.....	5
2.2.4 Operation of silicon strip detector.....	10
2.3 Effects of radiation defects and thermal donors in silicon.....	12
2.3.1 Radiation damage mechanisms.....	13
2.3.2 NIEL scaling hypothesis.....	13
2.3.3 Radiation defects.....	15
2.3.4 Thermal donors.....	16
2.3.5 Effects of defects on detector properties.....	16
2.3.6 Annealing.....	17
3. Methods.....	20
3.1 Device processing.....	20
3.1.1 Device structure.....	20
3.1.2 Process description.....	22
3.2 Irradiations.....	23
3.3 Characterizations.....	23
3.3.1 Current-voltage and the capacitance-voltage measurements.....	23
3.3.2 TCT measurement.....	25
3.3.3 DLTS measurement.....	28
3.3.4 Beam telescope tests.....	30
4. Results and discussion.....	34
5. Conclusions.....	37
References.....	38
List of Symbols.....	42
List of abbreviations.....	44

# 1. Introduction

Silicon strip detectors have been used in particle tracking applications in high-energy physics since the 1980's, but the Large Hadron Collider (LHC) experiments are the first ones to use silicon strip detectors on a large scale [1][2]. The search for the Higgs boson, which is a hypothetical, massive subatomic particle whose existence would explain the masses of the elementary particles [3][4], is the most important task for the LHC. Only few proton-proton collisions produce Higgs, so a very high luminosity is needed, causing a hostile radiation environment for the silicon devices. Unfortunately, the operational limits of the present devices made from standard Float Zone (FZ) silicon material will be reached at around  $1.6 \times 10^{14} \text{ cm}^{-2}$  1 MeV neutron equivalent fluence, which corresponds roughly to the fluence that strip detectors will receive in the inner barrel of the silicon tracker of the CMS (Compact Muon Solenoid) experiment in the LHC during ten years of operation [1]. That is, the radiation-damage-induced changes in the silicon bulk increase the leakage current and the depletion voltage and decrease the charge collection efficiency, finally leading to non-tolerable deterioration in the detector performance [5]. Therefore, another solution for the possible upgrade of LHC has to be found, since the fluencies of fast hadrons can reach  $10^{16} \text{ cm}^{-2}$  with the proposed luminosity of  $10^{35} \text{ cm}^{-2}\text{s}^{-1}$ .

The effects of the irradiation induced defects in the silicon strip detectors can be divided into three categories [5]. First, the defects introduce generation recombination centers that cause an increase in the detector leakage current. Second, the acceptor type defects compensate the initial space charge in the donor doped silicon that leads to the increase of the needed depletion voltage. The third effect is the deterioration of the charge collection efficiency, which is due to the trapping of the charge carriers.

The approaches to improve the radiation tolerance (radiation hardness) of silicon devices range from suitable defect engineering, i.e. deliberate modification of the detector bulk material, to operating the devices at cryogenic temperatures and designing special detector geometries, such as p-type detectors, epitaxial silicon detectors or 3D detectors. There is also extensive research activity concerning new detector materials such as SiC or diamond that could be extensively radiation hard. [6] However, the processing of these new materials is fairly difficult and their availability is rather poor in addition to their being relatively expensive. Therefore, at the moment, silicon seems to be the only economical choice for the large-scale applications with its good availability, easy and well-known processing and moderate price.

It has been proved that oxygen improves the radiation hardness of the silicon devices [7] [8]. The ROSE Collaboration developed the technique of oxygen-enriched Float Zone silicon (DOFZ), which results in an oxygen concentration of  $2 \times 10^{17} \text{ O/cm}^3$  in normal detector processing [9] [10]. However, this technique requires prolonged high temperature drive-in oxygen diffusion from  $\text{SiO}_2$  layers on the polished wafers: this procedure may lead to process induced contamination on the wafers. Since Czochralski silicon contains an intrinsically high level of oxygen, typically  $10^{17}$ - $10^{18} \text{ cm}^{-3}$ , it was investigated in the ROSE Collaboration as well as elsewhere. However, the resistivity of

the standard Czochralski silicon wafers that were investigated was insufficient for detector purposes and the material was considered an unsuitable option.

Only recently have the developments in the crystal growth technique of Czochralski silicon enabled the production of wafers with sufficiently high resistivity and a well controlled concentration of oxygen for particle detection applications. Helsinki Institute of Physics CMS Tracker group obtained from the Finnish Company Okmetic Ltd the high-resistivity Czochralski silicon wafers grown by the magnetic Czochralski method (MCZ) for the radiation hardness studies. The research was conducted in the framework of CERN RD50 Collaboration, the objective of which is to improve the radiation tolerance of semiconductor sensors used in high-energy physics experiments.

The publications presented in this thesis describe the radiation hardness properties of MCZ silicon detectors and reference FZ silicon detectors investigated by different characterization methods. The thesis is organized as follows. First, the theory of crystal growth techniques, silicon detectors and the effects of radiation defects and thermal donors in silicon is presented. Then, the methods involved in device processing, irradiations and characterizations, are described. The last chapters concentrate on the results, discussion of the subject and conclusions.

## 2. Theory

### 2.1 Silicon growth techniques

The particle detectors are typically processed on silicon wafers grown by the Float Zone (FZ) method because the wafers need to have high resistivity and high purity. Only recently have the developments in the crystal growth technique of Czochralski (CZ) silicon enabled the production of wafers with sufficiently high resistivity and well-controlled concentration of oxygen for particle detection applications.

#### 2.1.1 Float Zone silicon

##### Standard Float Zone silicon

In the Float Zone method, a high-purity polycrystalline silicon rod with a single-crystal seed of known orientation at the bottom is held in the vertical position and rotated around the axis. A radio-frequency (RF) heater melts a small zone of the rod, called the floating zone, in an argon atmosphere: as the RF-coil moves upwards, single-crystal silicon solidifies below the floating zone (Figure 1). As the molten silicon crystallizes, it follows the crystal structure of the seed crystal and thus single-crystal silicon of the required orientation is formed. In addition, as the solubility of many impurities is higher in the liquid than in the solid phase, the silicon is purified. The process can be repeated until sufficient purity (the acceptable concentration of metallic impurities in detector substrates is less than  $10^{10} \text{ cm}^{-3}$ ) is achieved: by this method it is possible to produce silicon with negligible oxygen concentration (typically below  $10^{15} \text{ cm}^{-3}$ ) and a resistivity of up to 30  $\text{k}\Omega\text{cm}$ .

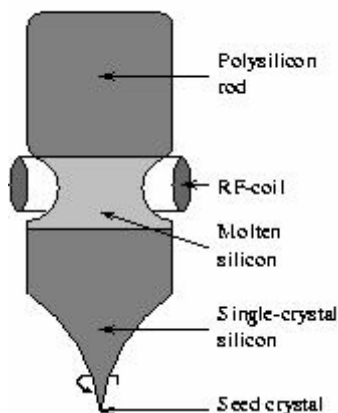


Figure 1. Float Zone silicon crystal growth method.

## Oxygenated Float Zone silicon

The resistance to radiation can be improved by having a high oxygen concentration in the silicon. Since in the Float Zone wafers the oxygen concentration is very low, the oxygen has to be incorporated into the material. This can be achieved either by modifications in the crystal growth or thermal diffusion from SiO<sub>2</sub> layers on polished wafers [11].

### 2.1.2 Czochralski silicon

#### Standard Czochralski silicon

In the Czochralski crystal growth method [12], the starting electronic grade polycrystalline silicon (EGS) is placed in a fused silica crucible (pure SiO<sub>2</sub>) with the desired dopant (either in a diluted form as silicon dopant alloy or in elemental form). The crucible is surrounded by a susceptor of a furnace. Then the silicon is melted in an inert atmosphere and a small seed crystal of known orientation is dipped into the molten silicon. Next the seed crystal is quickly withdrawn from the melt in order to form a thin neck for suppressing the dislocations caused by the temperature difference between the melt and the seed crystal. Then the pulling rate is lowered. During this process the seed crystal and the crucible are rotated in the opposite directions. This results in a formation of a large single crystal with the same characteristics as the seed.

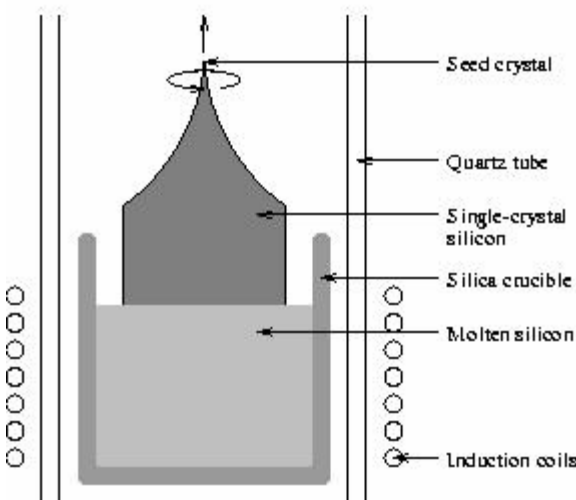


Figure 2. Czochralski silicon crystal growth method.

During the crystal growth, the silica crucible gradually dissolves releasing oxygen, carbon and other impurities, namely aluminum and boron, into the silicon melt. Most of the oxygen vaporizes from the melt as silicon monoxide (SiO) that is transported away by the protection gas, but the rest stays in the melt and can dissolve into the single-crystal. The concentrations of O and C impurities in the single crystal are typically  $1-10 \times 10^{17}$  and  $1-5 \times 10^{16}$  atoms/cm<sup>3</sup>, respectively. Thermal gradients present in the melt crucible

cause strong buoyancy-driven convection and surface-tension-driven flows at the free surfaces of the melt. These melt-convective flows are at least partially turbulent and are largely responsible for the crystal imperfections and radially and microscopically non-uniform distributions of dopant and impurity atoms in the crystals. In addition, the silicon melt gets richer in dopant atoms: therefore the ingot resistivity lowers as a function of the length of the ingot. For these reasons, the maximum resistivity of the standard Czochralski wafers is rather limited.

### **Magnetic Czochralski silicon**

The magnetic Czochralski (MCZ) method is in principle the same as the standard Czochralski crystal growth method, but the ingot is grown in a strong magnetic field [13], which is used to dampen the oscillations in the silicon melt [14]. That is, the Lorentz force resulting from the applied magnetic field influences the flow and reduces the amplitude of the melt fluctuations. In this method, the concentration and the distribution of the oxygen can be controlled better than in the standard CZ method, which is important for the large-area detector applications. The method is today widely used in the semiconductor industry: wafers grown using the magnetic Czochralski method have therefore become available for the detector applications also.

## **2.2 Silicon detectors**

A silicon strip detector is a reverse biased p-n junction diode, where the p-side of the junction is segmented into an array of narrow strips to achieve position sensitivity. Charged particles or photons traversing the detector create electron-hole pairs. The holes drifting in the electric field towards the negatively biased p-strips are collected as a charge pulse. Since the holes drift to the strip closest to them, it is possible to distinguish where the particle has crossed the detector, i.e. spatial resolution is obtained.

### **2.2.1 P-n junction**

The theory of the p-n junction presented in this chapter is based on references [15] and [16].

In order to explain the operation of a p-n junction, the formation of the junction can be thought of as bringing two originally isolated regions of opposite conduction type into intimate contact. When the regions are joined, a thermal equilibrium is established as equal numbers of mobile electrons and holes from the n-type and p-type recombine. This results in the formation of two regions that consist of immobile charges, since the electrons that exit the n-region leave behind positively ionized donor atoms and holes that exit the p-region leave behind negatively ionized acceptor atoms. The concentration

gradient causes an electric field that is directed from positive charge to negative charge and as the field increases, it inhibits further carrier flow across the junction. The electric field strength has its maximum at the junction and is zero at the edges of the depletion region. The conduction and valence bands are bent in the depletion region by the energy  $qV_{bi}$ , which is called the built-in potential.

The real p-n junction is approximately described by an abrupt junction (Figure 3), where the total net dopant density function changes stepwise from the acceptor atom density  $N_a$  in the p-region to the donor density  $N_d$  in the n-region. In particular, if  $N_a \gg N_d$ , a one-sided abrupt junction, i.e. a  $p^+$ -n junction, is obtained.

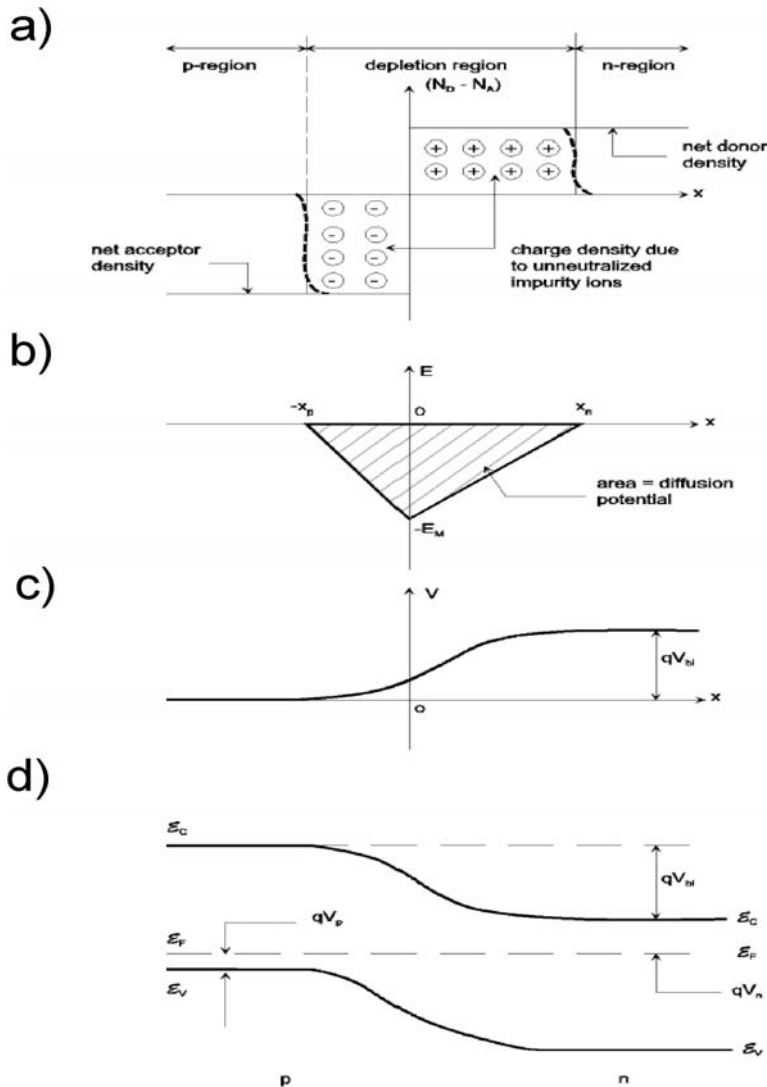


Figure 3. Abrupt p-n-junction in thermal equilibrium: a) space charge distribution of the abrupt junction, b) and c) electric field distribution and potential variation with the distance, d) energy band diagram of the system [15].

In the case of an abrupt  $p^+$ -n junction, one side of the junction is more heavily doped than the other. In thermal equilibrium with no external bias, the overall charge neutrality has

to be satisfied, and thus the depletion region of thickness  $W$  extends much further into the less doped side of the junction (Figure 3, b)). In particular, in the particle detectors the highly doped region is deposited on a high-resistivity substrate with low dopant concentration and, when sufficient reverse bias is applied, the depletion region spans over the whole thickness  $d$  of the detector up to the back contact. To simplify the analysis, it can be assumed that the device is fully depleted over the depletion region and the adjacent neutral regions contain no charge, which means that the space charge is constant in the region  $0 < x < W$ , where  $x$  denotes the distance. To simplify the calculation, we first consider the thermal equilibrium condition with no applied voltage and no current flow. The electric potential  $\phi$ , and the electric field  $E$ , can be calculated by solving the Poisson's equation:

$$-\frac{d^2\phi(x)}{dx^2} = \frac{\rho}{\epsilon\epsilon_0} = \frac{qN_{eff}}{\epsilon\epsilon_0}, \quad (1)$$

where  $\rho$  denotes the space charge density,  $\epsilon\epsilon_0$  the permittivity of silicon,  $q$  the elementary charge and  $N_{eff}$  the effective doping concentration. With the boundary condition:

$$E(x=W) = -\frac{d}{dx}\phi(x=W) = 0, \quad (2)$$

a first integration of (1) gives an expression for the electric field strength that depends linearly on  $x$  and that reaches the maximum field strength at the  $p^+$ - $n$  interface, where  $x=0$ :

$$E_{max} = -\frac{qN_{eff}}{\epsilon\epsilon_0}W. \quad (3)$$

A second integration with the boundary condition  $\phi(x=W) = 0$  leads to:

$$\phi(x) = -\frac{1}{2}\frac{qN_{eff}}{\epsilon\epsilon_0}(x-W)^2 \quad \text{for } 0 \leq x \leq W \text{ and } W \leq d. \quad (4)$$

In thermal equilibrium, the reverse voltage  $V$  equals the built-in potential across the depletion region. Therefore with the condition  $\phi(x=0) = -V_{bi}-V$ , the depletion depth can be expressed as:

$$W = \sqrt{\frac{2\epsilon\epsilon_0}{q|N_{eff}|}(V + V_{bi})} \quad \text{for } W \leq d. \quad (5)$$

With increasing reverse bias, the electric field expands until it reaches the back contact ( $W=d$ ). The corresponding voltage is called the depletion voltage  $V_{dep}$ , or the operation

voltage, of the detector.  $V_{dep}$  is connected with the effective doping concentration  $N_{eff}$  through the relation:

$$V_{dep} + V_{bi} = \frac{q}{2\epsilon\epsilon_0} |N_{eff}| d^2. \quad (6)$$

It is desirable to operate the detector with relatively low bias voltage. From equation (6) it is evident that this can be achieved either by lowering the doping concentration of the substrate or decreasing the device thickness.

The dynamic junction capacitance is defined as  $C=dQ/dV$ , where  $dQ$  is the incremental change in the depletion layer charge for an incremental change in the applied voltage  $dV$ . The space charge  $Q$  is given by  $Q=qN_{eff}AW$ , where  $A$  denotes the area of the device.  $dQ$  gives  $qN_{eff}AdW$  and

$$C = \frac{dQ}{dV} = \frac{dQ}{dW} \frac{dW}{dV}. \quad (7)$$

The derivative of equation (5) with respect to  $V$  and the above relation give the junction capacitance:

$$C(V) = \epsilon\epsilon_0 \frac{A}{W} = A \sqrt{\frac{\epsilon\epsilon_0 q |N_{eff}|}{2(V + V_{bi})}} \quad \text{for } W \leq d \text{ and } V \leq V_{dep}. \quad (8)$$

With increasing voltage, the capacitance decreases with  $C \propto 1/\sqrt{V}$  and, at the full depletion, reaches a value of:

$$C_{geo} = \frac{\epsilon\epsilon_0 A}{d}. \quad (9)$$

This is called the geometrical capacitance because it depends only on the geometrical size of the device. Higher voltages than the depletion voltage will not change the depletion depth anymore, therefore the capacitance stays constant.

In the reverse biased junction, the current is dominated by the carrier generation current in the depletion region. Since only the defects located in the space charge region contribute to the bulk generation current, it depends on the voltage the same way as the width of the depleted zone:

$$I_{bulk} \propto W \propto \sqrt{V} \quad \text{for } V \leq V_{dep} \quad (10)$$

and saturates when the applied voltage reaches the full depletion voltage. The bulk generation current is often described by the generation lifetime  $\tau_g$ :

$$I_{bulk} \propto \frac{qn_i W}{\tau_g}, \quad (11)$$

where the  $\tau_g$  is defined as:

$$\tau_g = \frac{\sigma_p \sigma_n v_{th} N_t}{\sigma_n \exp\left(\frac{E_t - E_i}{k_B T}\right) + \sigma_p \exp\left(\frac{E_i - E_t}{k_B T}\right)}, \quad (12)$$

where  $v_{th}$  is the thermal velocity,  $N_t$  the defect density,  $\sigma_p$  and  $\sigma_n$  the hole and electron capture cross-sections, respectively,  $E_t$  the defect energy level,  $E_i$  the intrinsic energy level,  $k_B$  the Boltzmann's constant and  $T$  the absolute temperature. As can be seen from (12), the  $\tau_g$  is determined by the density of localized energy states giving rise to the generation processes: it can therefore be used to evaluate the purity of the silicon crystal. The  $n_i$  in (11) is the intrinsic carrier concentration of the silicon, which is given by:

$$n_i = \sqrt{N_c N_v} e^{-\frac{E_g}{2k_B T}}, \quad (13)$$

where  $N_c$  is the effective density of states in the conduction band,  $N_v$  is the effective density of states in the valence band and  $E_g$  the band gap of silicon. At room temperature (300K)  $n_i \cong 10^{10} \text{ cm}^{-3}$ . The  $n_i$  has very strong temperature dependence due to the exponent  $-E_g/2k_B T$ . For this reason, when the leakage current measurements are compared, they are scaled to a particular reference temperature by the equation:

$$I(T_c) = I(T_m) \left(\frac{T_c}{T_m}\right)^2 e^{-\frac{E_g}{2k_b} \left(\frac{1}{T_c} - \frac{1}{T_m}\right)}, \quad (14)$$

where  $T_c$  is the comparison temperature and  $T_m$  the measurement temperature.

The breakdown of the reverse biased junction occurs when a sufficiently high field is applied to the p-n junction and it starts conducting a very large current. There are basically two mechanisms by which a junction breakdown can happen in a reverse biased p-i-n-diode: tunneling and avalanche multiplication. Since the probability for electron tunneling in silicon becomes significant only when the electric field approaches  $10^6 \text{ V/cm}$ , it is not considered to be a relevant mechanism for a particle detector.

The avalanche breakdown occurs when the electric field in the depletion region becomes so high that the charge carriers gain enough kinetic energy to ionize electron-hole pairs, when they collide with an atom in the silicon crystal. For a one-sided abrupt p<sup>+</sup>-n junction, the reverse breakdown voltage  $V_B$  can be approximated by:

$$V_B = \frac{E_B W}{2} = \frac{\epsilon \epsilon_0 E_B^2}{2qN_D}, \quad (15)$$

where  $E_B$  is the value for the electric field critical to breakdown and  $N_D$  the donor doping density of the n-type bulk material. Since the bulk is very lightly doped in particle detectors, the breakdown voltage is mainly determined by the geometry of the p-n structure. Since the electric field tends to concentrate on the corner points, the electrode geometry has a strong influence on the breakdown voltage. Therefore, the strip implants in the particle detectors are heavily boron doped and diffused deep into the n-type bulk.

#### 2.2.4 Operation of silicon strip detector

The small ionization energy of silicon makes it very useful as a detector material. For the particles interacting with silicon, the energy required to create an electron-hole pair is 3.6 eV. The band gap of silicon is 1.12 eV at room temperature and the average energy needed to create a single pair, called the radiation ionization energy, is empirically found to be about three times the band gap energy of the semiconductor [17]. This is due to the phonon excitation, which is required for momentum conservation. A minimum ionizing particle (MIP, a particle that has high energy and low mass and whose energy loss per unit path length is small, e.g. 3 MeV proton or cosmic ray muon) most probably deposits an energy of 90 keV in a 300  $\mu\text{m}$  thick silicon detector, which means approximately 25000 electron-hole pairs [19].

In a p-n junction detector structure, the whole detector bulk is active volume. The  $p^+$  strips are implanted on the front-surface and the  $n^+$  region is implanted on the back side of the wafer as shown in Figure 4. In the modern high-energy physics experiments, the bunch-crossing interval is in the order of tens of nanoseconds. Thus, charge collection by the diffusion is too slow a process to collect the particle generated carriers. Therefore, the detector bulk is fully depleted by reverse bias and the charge collection is based on the drifting of carriers. Once an MIP hits a detector, the created electrons and holes are separated by the electric field in the depletion region, i.e. the holes drift to the negatively biased  $p^+$  strips and the electrons to the positively biased  $n^+$  ohmic contact on the back side, and they create a current pulse, which is registered by the readout electronics (Figure 4). Since the charge collection time in the detector itself is very short, i.e. in the order of 20 ns, the signal readout speed is mainly determined by the speed of the readout electronics.

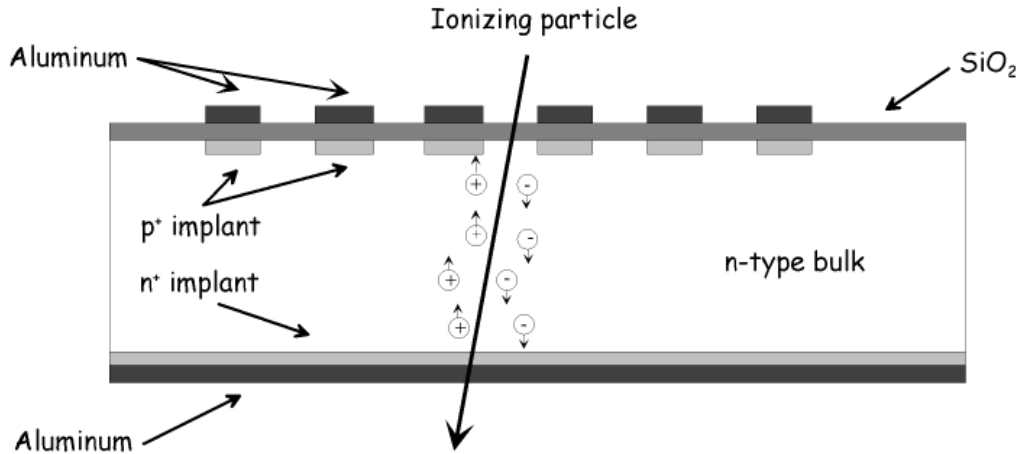


Figure 4. Cross-section of a silicon strip detector.

Traditionally the signal readout electronics are connected directly to the p+ strips (DC coupling). In a DC-coupled detector, the leakage current is also connected to the readout. Therefore, in the modern, so-called “AC-coupled”, detectors this is prevented by using a simple high-pass filter, i.e. the p+ strips are connected to the bias line (Figure 5, d)) through protective resistors (bias resistors, Figure 5, c)) that conduct the leakage current to the common bias line and the signal current is measured through the strip capacitors (Figure 5, a)).

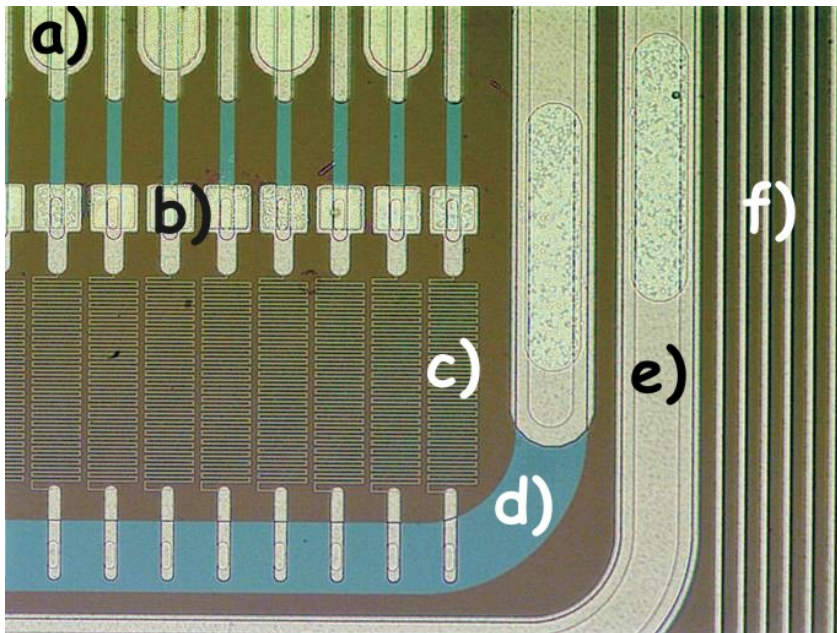
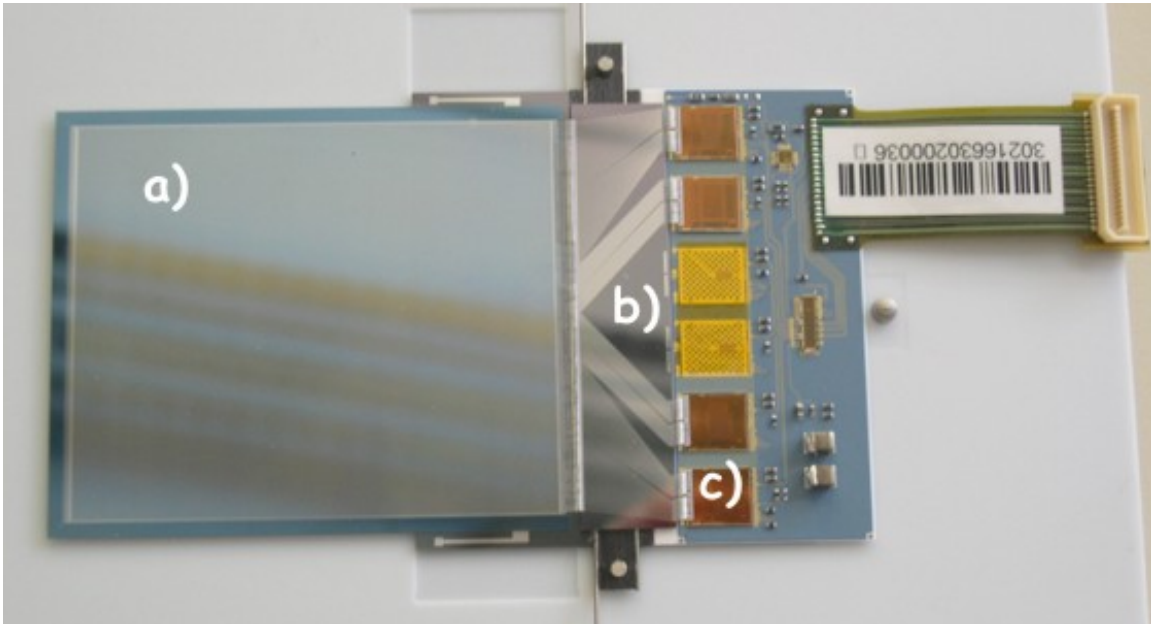


Figure 5. AC-coupled detector: a) AC-pad from which the signal current is measured and which is bonded to the readout electronics, b) DC-pad for testing purposes, c) bias resistor, d) bias line, e) guard ring and f) multi guard ring structure typically used in the detectors.



**Figure 6. Silicon strip detector module with readout electronics: a) strip detector, b) pitch adapter and c) readout chip. The strip detectors can have different strip pitches, depending on the application. The strip adapter is used to match the strips of the detector to the input channels of the readout chips.**

### ***2.3 Effects of radiation defects and thermal donors in silicon***

The main effects of the irradiation-induced defects can be divided into three categories. First, the defects introduce generation recombination centers that cause an increase in the detector leakage current. Second, the acceptor-type defects compensate the initial space charge in the donor doped silicon that leads to the changes in the effective doping concentration and in the operation voltage needed to fully deplete the detector thickness. The third effect is the deterioration of the charge collection efficiency, which is due to the trapping of the charge carriers.

It has been noted that the defects are subject to changes after long-term storage at room temperature. Such annealing effects may be caused by changes due to the dissolution of the clusters, i.e. the migrating vacancies and interstitials released in the process. Since the observed time constants for the annealing processes are rather large – in other words, since the evolution in the electrical characteristics continues for years at the room temperature – the aging effect is typically stimulated by increasing the temperature.

### 2.3.1 Radiation damage mechanisms

In the detectors radiation damage occurs through two basic mechanisms: bulk damage, which is due to the displacement of atoms from their lattice sites, and surface damage, which is due to the charge build-up in the surface layers of the devices.

#### Surface damage

Ionizing radiation creates holes in the surface oxide layers of the silicon detectors. These holes become trapped in the oxide or interact with the atoms at the silicon-oxide interface to form interface states [18]. The trapping results in the increase of the positive charge in the oxide and therefore degrades the oxide quality, while the interface states give rise to new energy levels in the forbidden band gap. These changes can lead to decreased inter-strip isolation that causes unwanted signal charge sharing and increased inter-strip capacitance. However, these effects are strongly dependent on the device structure and the fabrication details [19]. Thus, with the careful choice of fabrication technology and geometry, the changes in the device behavior can be minimized.

#### Bulk damage

Bulk damage is caused by non-ionizing interactions of the high-energy particles. These particles, e.g. hadrons or gammas, cause bulk damage in silicon, mainly by displacing a Primary Knock-on Atom (PKA) out of its lattice site [9]. Such single displacement results in a pair of an interstitial atom and a left-over vacancy (Frenkel pair). For neutrons and electrons, the threshold energies for the pair formation are 170 eV and 260 keV, respectively. Low-energy recoils above these thresholds and below 5 keV will most probably create point defects. However, if the energy transferred to the PKA is high enough, it can displace other lattice atoms from their lattice sites before stopping. These can further displace other atoms creating a displacement cascade that forms an agglomeration of defects, i.e. defect clusters at the end of the PKA track. The kinematic thresholds for the cluster production are ~35 keV for the neutrons and ~8 MeV for the electrons. Hence, the observed bulk damage does not depend only on the energy of the particle but also on its type. Both point defects and defect clusters can seriously affect the detector performance, depending on their concentration, energy level and the respective electron and hole capture cross-section [9].

### 2.3.2 NIEL scaling hypothesis

The Non-Ionizing Energy Loss (NIEL) refers to the fraction of the energy that the incident particle transfers to the lattice by non-ionizing means, e.g. elastic scattering. This energy, which is released to the matter, is responsible for the displacements of the atoms in the crystal lattice. The observed deterioration effects depend on the fluence, the

particle type and the energy. The proportionality between the NIEL-value and the resulting damage effects is referred to as the NIEL-scaling hypothesis and the NIEL values are used to normalize the different effects expected from various particles over large energy regions [20] [21].

The basic assumption in the NIEL-scaling hypothesis is that any displacement-damage induced change in the material scales linearly with the amount of the energy imparted in the collision. The NIEL value can be expressed by the displacement damage cross-section  $D$ . Since the  $D$  is normally given in  $MeVmb$  and the NIEL value in  $keVcm^2/g$ , for silicon with atomic mass  $A = 28.086 u$ , the relation between the  $D$  and the NIEL is:  $100 MeVmb = 2.144 keVcm^2/g$ . On the basis of the NIEL scaling, the damage efficiency of any particle with a given kinetic energy  $E$  can be described by the hardness factor  $\kappa$ , defined as

$$\kappa_{particle}(E) = \frac{D_{particle}(E)}{D_n(E=1MeV)}, \quad (16)$$

where  $D_{particle}$  is the displacement damage cross-section of the particle [21] and  $D_n$  the displacement damage cross-section for 1 MeV neutrons. By the ASTM standard, the  $D_n$  is set as a normalizing value  $D_n(E=1MeV) = 95 MeVmb$ . That is, any particle fluence can be reduced to an equivalent 1 MeV neutron fluence producing the same bulk damage in the specific material. In Figure 7, the initial distributions of vacancies produced by 10 MeV protons, 24 GeV protons and 1 MeV neutrons, corresponding to a fluence of  $10^{14} cm^{-2}$ , are presented. The picture demonstrates well how the hardness factor  $\kappa$  is determined, i.e. 10 MeV protons create 36824 vacancies and 1 MeV neutrons 8870 vacancies, which corresponds to the hardness factor of 4.2 [21] [22].

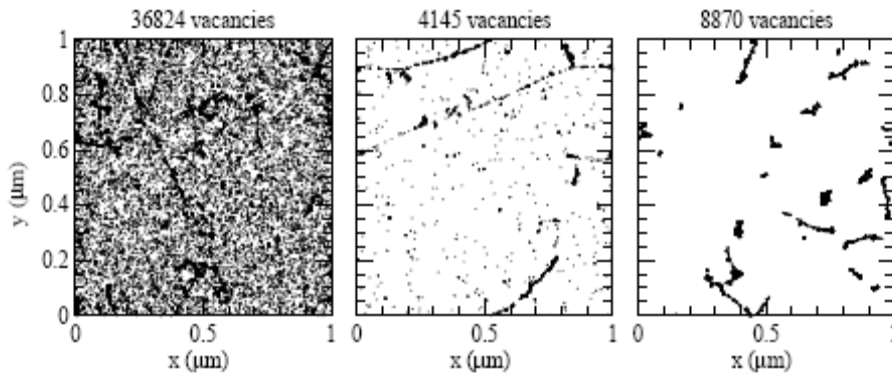


Figure 7. The initial distribution of vacancies produced by 10 MeV protons (left), 24 GeV protons (middle) and 1 MeV neutrons (right). The plots are projections over  $1 \mu m$  of depth ( $z$ ) and correspond to a fluence of  $10^{14} cm^{-2}$  [22].

The NIEL scaling is regularly used for making a comparison between the damage results produced in the test experiments with different particles and energies. In addition, the damage predictions of the large-scale experiments are often based on the NIEL scaling. However, there is still no microscopic understanding of why the damage should scale

with NIEL, and there is evidence that even significant violations of the NIEL scaling can be consistent with the experimental data [22][23]. It has been argued that the real damage depends not only on the NIEL value, but also on the specifics of the occurring energy transfers that are not fully described by the NIEL values. Therefore, one has to be cautious when applying the NIEL scaling. It cannot be used as a strict rule, but as a tool to cancel out most of the particle and energy dependences of the observed damage in silicon detectors [24]

### 2.3.3 Radiation defects

Different kinds of defects are created in the silicon bulk depending on the energy and type of the irradiation. These defects are categorized as clusters and point defects. Light particles such as photons, as well as low-energy electrons, produce only point defects, low-energy protons (< 50 MeV) produce both clusters and point defects, high-energy protons mostly clusters and neutron irradiation mainly clusters [22].

The point defects are divided into interstitials and vacancies that can be thought of as the primary displacement defects. They are essentially unstable and mobile at room temperature. Most of the vacancies recombine with the interstitials. Some of the remaining vacancies form di-vacancy or multi-vacancy defect complexes and the rest of the vacancies and interstitials diffuse through the crystal. During this migration they react with other defects or impurity atoms present in the silicon crystal and form stable complexes.

The exact internal structure of clusters is unclear, even though it is known that they are composed of interstitials and vacancies. The initial concentration of vacancies and interstitials is very high inside the cluster and most of these vacancy-interstitial pairs are annihilated in a very short timescale. The clusters are thought to be responsible for the significant differences seen in the damage produced by the light particles and heavy particles. The introduction rate of di-vacancy or multi-vacancy defects is much higher with heavy particle radiation than with for example gamma radiation. This is thought to be due to the high vacancy density inside clusters, since there is evidence that the di- or multi-vacancies are created by the vacancies in the vicinity of each other, rather than by the vacancies related to different displacement events. The light particles are able to displace only individual silicon atoms from their lattice sites: thus it is unlikely that a di- or multi-vacancy complex would form. In addition, cluster defects are thought to have an important role in explaining why oxygenation improves the radiation hardness of materials towards charged hadrons [24]. The oxygen captures vacancies, suppresses phosphorus removal and encourages vacancy-oxygen (VO) complex formation at the expense of di-vacancy oxygen ( $V_2O$ ) or  $V_3O$  complexes. The VO complex is relatively harmless because its energy level is distant from the mid-band gap: its formation is therefore beneficial compared to the  $V_2O$  and  $V_3O$  that are thought to be deep-level acceptors [25].

### **2.3.4 Thermal donors**

It is well known that if a silicon wafer with high oxygen concentration undergoes heat treatments in certain temperatures, the effective doping concentration of the material can seriously change. This is due to the formation of electrically active centers that are related to the oxygen and act as donors. These donors are called thermal donors (TDs) because of their generation under thermal treatment. They are formed in the temperature range of 350-550°C and again in the range of 600-700°C (so-called new donors) [26] [27].

The two most important factors that control the TD formation are the duration and the temperature of the heat treatment. At temperatures below 450°C, considerably smaller rates of TD formation are observed and the saturation concentration is less than for treatment at 450°C. On the other hand, the donor states can be annihilated by subsequent heat treatment above 800°C and the formation is greatly reduced in the subsequent heat treatment at 450°C. Heating of the silicon for twenty hours at 1100°C stabilizes the material and no further donor states can be produced [26] [27] [28]. It has also been found that the impurities affect the oxygen donors, e.g. nitrogen can slightly inhibit the TD formation and react with oxygen to generate nitrogen-oxygen complexes as shallow thermal donors [29]. Therefore, the temperature treatment steps in the detector manufacturing process and the impurities present are critical to the final electrical properties of the device.

### **2.3.5 Effects of defects on detector properties**

The effects of radiation on the detector performance are due to the stable defects that are formed when the primary displacement defects (vacancies and interstitials) react with other defects or impurities. Some of these stable complexes are electrically active and several of these defects have been identified by means of different measurement techniques such as Deep Level Transient Spectroscopy (DLTS) or Thermally Stimulated Current (TSC).

The defects can be classified by their electrical properties as acceptors, donors and amphoteric defects, as shallow and deep levels or as electron and hole traps. Defects that have energy levels in the band gap can capture and emit electrons and holes. Acceptor type defects are negatively charged when they are occupied by an electron, while donors are in that case neutral. Some of the defects have more than one level in the band gap. These are called amphoteric defects and have an acceptor and donor level in the band gap. In the space charge region, usually levels in the lower half of the band gap are occupied with electrons, while in the upper half they are not. This means that, if a donor exists in the lower half of the band gap or an acceptor in the upper half, they are neutral in the space charge region and vice versa, respectively. If an acceptor exists in the lower half of the space charge region and donor in the upper half, they are ionized and introduce a negative and positive space charge, respectively. Very often, the acceptors and donors are called shallow if they are close to the conduction/valence band edge. Since the charge

state of a level in thermal equilibrium is ruled by the Fermi-level position, it depends on the conduction type and the doping concentration of the material. Therefore, the same defect acts as shallow in one material and deep in another. In addition, every defect can trap electrons and holes: the terms electron and hole traps originate from the characterization methods that are based on the junction space-charge technique (DLTS, TSC).

The deep energy levels near the middle of the band gap can act as generation and recombination centers and are thus responsible for an increase in the detector leakage current. It has been found experimentally that the leakage current increases linearly with the fluence [9] [30]. Since the process of carrier generation via the deep levels is an activated process, the resulting leakage current is very sensitive to temperature, i.e. the leakage current decreases exponentially with decreasing temperature. This problem can therefore be reduced by cooling the detectors.

The removal of dopants by the formation of complex defects, as well as the generation of charged centers, changes the effective doping concentration and needed voltage to fully deplete the detector thickness. The dominant acceptor type defects are able to compensate the initial space charge on the donor doped n-type silicon and the doping concentration decreases progressively as a function of the received fluence until the inversion to p-type happens. After the conductivity type inversion, the p-type effective doping concentration starts to increase linearly with the fluence. As a result, the needed depletion voltage of the device changes and finally reaches the breakdown voltage limit. In addition, the power consumption of the device increases, since both the needed voltage and the leakage current increase as a function of the radiation.

Defects also act as trapping centers for the electrons and holes that are created by the particles. Thermal excitation releases the trapped charge, but the effect still increases the charge collection time, and when the de-trapping time becomes longer than the measurement time, some of the charge carriers are lost, which results in reduced charge collection efficiency (CCE). Further irradiation increases the concentration of trapping centers and the reduction of the collected charge becomes significant. Together with the increased noise, this leads to a worsened signal-to-noise ratio (SNR), until finally it is not possible to distinguish the signal from the noise anymore [31][32].

### **2.3.6 Annealing**

It has been noted that the defects are subject to changes after long-term storage at room temperature. In silicon, vacancies and interstitials are essentially unstable and interact via migration, recombination and annihilation, or by producing other defects. In addition, certain impurities can trap interstitials and vacancies thereby forming stable complexes. In other words, the system seeks a natural equilibrium.

It is supposed that the radiation produces equal concentrations of vacancies and interstitials that are higher than the corresponding thermal equilibrium concentrations characteristic of each temperature. An important part of the vacancies and interstitials annihilate. Since the interstitials are much more mobile in silicon than the vacancies (their migration activation energy is a factor of two smaller than that of vacancies), the concentration of interstitials decays much more rapidly than that of vacancies. In the model proposed by Lazanu & Lazanu [33] that uses 20°C, the self-annealing corresponding to vacancy-interstitial annihilation and interstitial migration to sinks happens during the first 0.2 s, the vacancy-phosphorus complex formation and decomposition during  $10^4$  s and the di-vacancy-related annealing during  $10^7$  s. The annealing effects can also be classified as short term beneficial annealing, as a stable damage part and as reverse annealing [9]. In the detectors, during beneficial annealing, the effective doping concentration  $N_{eff}$  decreases until it reaches the local minimum. At this point, the depletion voltage and the leakage current are at their minimum after the irradiation. After this point, the  $N_{eff}$  starts to increase again, and the annealing turns into reverse annealing, as indicated in Figure 8.

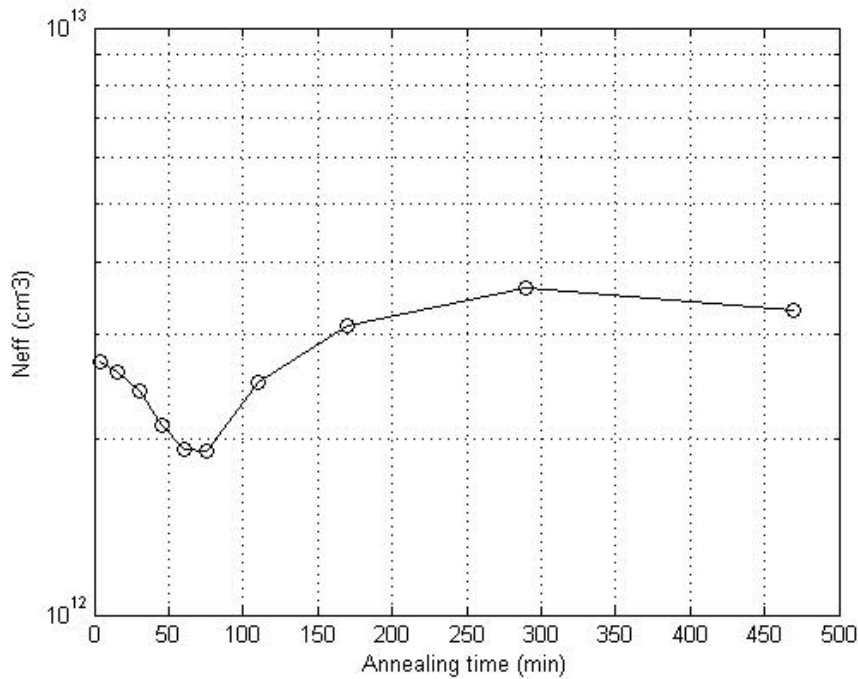


**Figure 8.** The evolution of the effective doping concentration as a function of annealing time at 80°C. The magnetic Czochralski silicon test diode was irradiated to  $1.6 \times 10^{14} \text{ cm}^{-2}$  1 MeV neutron equivalent fluence by 20 MeV protons. The  $N_{eff}$  values are extracted from  $V_{dep}$  measured by the capacitance-voltage method.

The time constants for the annealing process have been found to be independent of the irradiation fluence [9]. However, since they are rather large at room temperature, i.e. the evolution of the electrical characteristics continues for years at room temperature, the ageing effect is typically stimulated by increasing the temperature (Figure 8). It is possible to transfer the annealing function obtained at high temperature to a room

temperature measurement using an acceleration factor, which for an annealing at 80°C for 4 minutes, for example, equals roughly 7400 minutes at the room temperature [34]. Accordingly, a low temperature decreases the annealing rate: therefore the cooling of the detectors in the high-energy physics experiments also affects their annealing behavior.

### 3. Methods

The silicon strip detectors and pad detectors were chosen as test structures, because of their relatively easy manufacturing process that contains only a few thermal oxidations, ion implantations and sputter depositions. In order to have a reference, devices were processed on standard Float Zone silicon wafers in addition to Czochralski silicon wafers.

The devices were irradiated to various fluencies with low- and high-energy protons, neutrons and gamma rays, in order to see the effects of different particles on the device behavior. The electrical characteristics of the devices were measured by several different methods in different laboratories.

#### 3.1 Device processing

The detectors were processed at the clean room and fabrication facilities of the Microelectronics Centre of Helsinki University of Technology (MEC) by our research group. This allowed flexibility in the time scale, design and material choices compared to an industrial manufacturing process. In addition, this allowed testing different process parameters and their effects on the device properties.

##### 3.1.1 Device structure

The simple fabrication process of the detectors consisted of two thermal oxidations, two ion implantations and three sputter depositions. It was realized with five mask levels, four of which were used for patterning the active device regions and one was used for patterning the alignment marks. A more thorough process description can be found in [35].

The starting materials for the Czochralski silicon detectors were 4" single-side-polished 380  $\mu\text{m}$  and 300  $\mu\text{m}$  thick n-type  $\langle 100 \rangle$  wafers with a nominal resistivity of 900  $\Omega\text{cm}$  and 300  $\mu\text{m}$ -thick p-type  $\langle 100 \rangle$  wafers with a nominal resistivity of 1.9  $\text{k}\Omega\text{cm}$ . The wafers were grown using the magnetic Czochralski (MCZ) method by Okmetic Ltd, Finland and their oxygen concentration was  $4.9 \times 10^{17} \text{ cm}^{-3}$  measured by the Fourier Transform Infrared (FTIR) method. For reference purposes, detectors were also processed on 4" single-side-polished 300  $\mu\text{m}$ -thick n-type  $\langle 100 \rangle$  Float Zone wafers from Wacker with a resistivity of 1.2-1.3  $\text{k}\Omega\text{cm}$  and on 4" single-side-polished 520  $\mu\text{m}$ -thick n-type  $\langle 100 \rangle$  Float Zone wafers from Topsil with a resistivity of 2-3  $\text{k}\Omega\text{cm}$ .

In the strip detector design, the width of one  $\text{p}^+$ - strip was 10  $\mu\text{m}$ , the strip length 6.159 cm, and the strip pitch 50  $\mu\text{m}$ . The number of strips was 1024, resulting in a total detector area of 32.5  $\text{cm}^2$ . The strip insulator needed for the AC-coupling was made by dry

oxidizing a 200 nm thick silicon dioxide dielectric insulator between the p<sup>+</sup>-implant and the strip metallization. In order to reverse bias the p<sup>+</sup>-strips and to deplete the n-type bulk from charge carriers, a tungsten nitride (WN<sub>x</sub>) thin-film resistor (900 kΩ ± 5%) was processed between each strip and the common bias line. Tungsten nitride (WN<sub>x</sub>) bias resistors were chosen in order to avoid the high-temperature processing steps required for the traditional polysilicon bias resistors, since they might cause thermal donor formation. Besides, the WN<sub>x</sub> resistors are not type dependent and they could be used with both p- and n-type detectors. In addition, a structure of five guard rings surrounded the active detector area. In Figure 9, it is possible to see the bias resistors between the strips and the bias line, the bonding pads and two guard rings in a partial picture of the silicon strip detector.

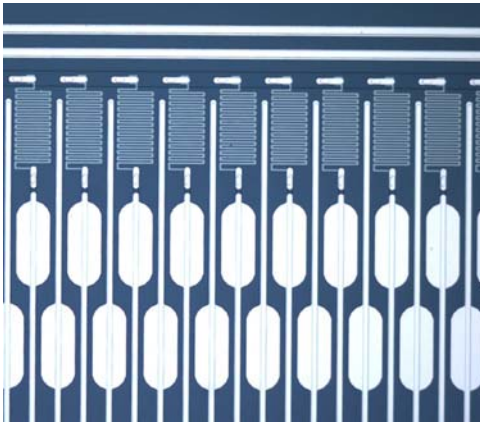


**Figure 9. Microscope picture of an AC-coupled silicon strip detector.**

The pad detectors (test diodes) were fabricated with essentially the same process parameters. However, the process steps required for bias resistors formation were not performed to the diode wafers. The diodes were of two different designs, the earlier versions had p<sup>+</sup> implanted area of 6 mm by 6 mm with two guard rings surrounding the active area and the later ones with an active pad implanted area of 5 mm by 5 mm surrounded by one 100 μm guard ring and sixteen 16 μm wide guard rings. In addition, in the newer design, a 1 mm diameter opening was left for the Transient Current Technique (TCT) measurements.

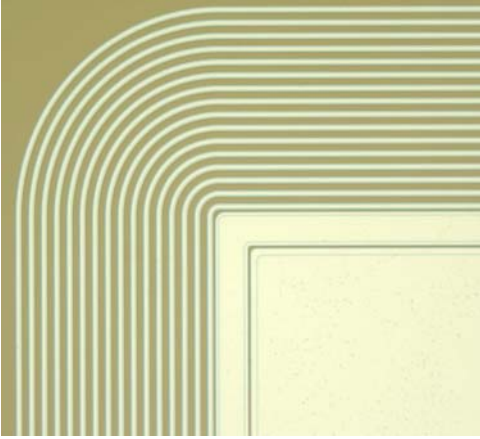


Figure 10. Corner of a diode with 16 guard rings.

### 3.1.2 Process description

#### Masking oxide

The first processing step is to grow a silicon dioxide ( $\text{SiO}_2$ ) layer. This layer serves as a mask during the ion implantation of the  $\text{p}^+$ -strips and protects the non-active area against contamination during the processing. Prior to the oxidation, the wafers are cleaned using the RCA (Radio Corporation of America) method in order to remove unwanted impurities from the surface. The 250 nm oxide layer is grown in a horizontal quartz tube furnace in a dry oxygen atmosphere at  $1050^\circ\text{C}$  over a period of approximately eight hours.

#### Formation of $\text{p}^+$ -strips and $\text{n}^+$ backside

The first-level photo mask is used for patterning the openings for the front-side  $\text{p}^+$ -strips. The ion implantation openings are patterned by buffered hydrogen fluoride (BHF) wet etching, which does not affect the silicon. After the etching, the wafers are ion implanted. First the front side is implanted with boron and then the back side with phosphorus using doses of  $10^{15}$  ions/ $\text{cm}^2$  and implantation energies of 30 KeV and 70 KeV, respectively. After the implantation, the masking oxide layer is removed by etching with BHF for 5 minutes. Finally, the field oxide layer is grown in a dry oxygen atmosphere at  $1050^\circ\text{C}$  for five hours. During the oxidation, the implanted boron and phosphorus ions also diffuse to their final depths.

#### AC-coupling and bias resistors

First, a layer of tungsten nitride ( $\text{WN}_x$ ) is sputtered on the front side of the wafers. Then, the bias resistors are patterned by photolithography and wet etched with a solution containing hydrogen peroxide and de-ionized water (1:1), which does not damage the underlying field oxide layer.

## **Contact openings**

Contact openings that are needed for making the electrical contacts with the implanted areas are patterned with the third mask. Then, the contact holes are opened by wet etching with BHF for 4 minutes.

## **Metallic contacts**

First, a 500 nm aluminum layer is sputtered on the front side of the wafer. Then, the aluminum layer is patterned with the fourth photo mask and wet etched with PS70-10 aluminum etching solution (Merck Electronic Chemicals Ltd.). Next, a 200 nm aluminum layer is sputtered on the back side of the wafer. After this, the aluminum is sintered by heating the wafer to 370°C for 30 minutes in a nitrogen atmosphere.

## **3.2 Irradiations**

The devices were irradiated to various fluencies with low- and high-energy protons, neutrons and  $^{60}\text{Co}$  gamma rays in different facilities: with 10 and 20 MeV protons at the Jyväskylä University Accelerator Laboratory [37], with 24 GeV protons at CERN [38], with 1 MeV neutrons at the University of Massachusetts [39] and  $^{60}\text{Co}$  gamma rays at the Brookhaven National Laboratory [40]. The gamma, neutron and 24 GeV proton irradiations were performed at ambient room temperature and the 10 MeV and 20 MeV proton irradiations at -10°C.

## **3.3 Characterizations**

In this work, the most important parameters of silicon detectors were measured with current-voltage (IV) measurement, capacitance-voltage (CV) measurement, transient current technique (TCT), deep-level transient spectroscopy (DLTS) and reference beam telescope. The CV- and IV-characteristics were measured at the CERN Solid State Detector Laboratory, the Brookhaven National Laboratory and the University of Karlsruhe. The TCT measurements were conducted at the Brookhaven National Laboratory. The DLTS measurements were carried out at the Ioffe Institute. The beam tests were conducted at the CERN H2 experimental area.

### **3.3.1 Current-voltage and the capacitance-voltage measurements**

The current-voltage and capacitance-voltage measurements are important basic characterization tools for irradiation effects. They are carried out with a semi-automatic

probe station inside a black box that protects the sample from light. The setup consists of a voltage source, current meter and capacitance meter, which are controlled by a computer. The sample is placed on the vacuum chuck that has an X-Y motion capability, while the adjustable probe needles make the electrical contact with the surface of the test structure (see Figure 11).

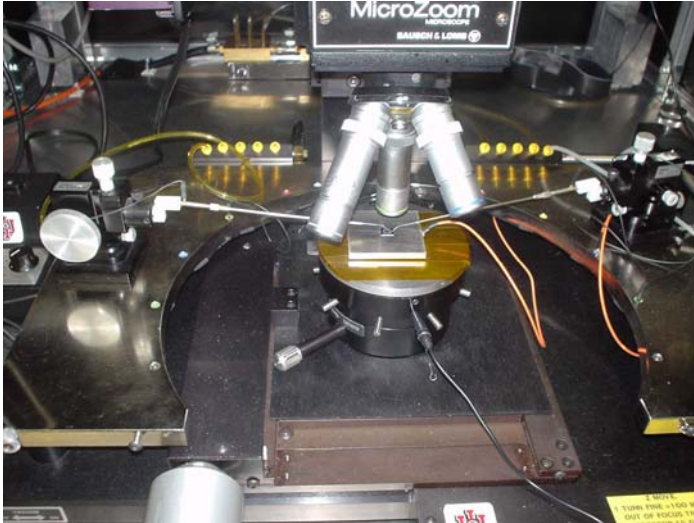


Figure 11. Test diode placed inside a probe station.

#### IV-measurement

In the current-voltage measurement, the total current of the detector is measured as a function of the applied bias voltage. A reverse bias voltage is applied to the back surface of the detector and the current ( $I_{leak}$ ) between the back side and the front side of the detector is monitored. If the guard ring of the device is kept in the same potential as the contact pad, the guard ring collects the leakage current from the edges of the device and the measured current corresponds to the real bulk current arising from the detector active volume. In the non-irradiated detectors, the  $I_{leak}$  is dominantly bulk generation current (see equation (11)), and thus is strongly temperature dependent. The measurement temperature is therefore an important variable and has to be known in order to produce comparable results (equation (14)).

#### CV-measurement

The capacitance-voltage measurement is used to determine the depletion voltage ( $V_{dep}$ ) of the detector. A reverse bias voltage is applied to the device and the capacitance between the back side and the front side is measured as a function of the bias voltage. When the CV-data graph is plotted on a double logarithmic scale of voltage and capacitance, the  $V_{dep}$  can be found at the turning point of the resulting graph, where the capacitance starts saturating as explained in the theory chapter. Figure 12 presents the CV-data graphs of 500  $\mu\text{m}$  thick Float Zone silicon and 380  $\mu\text{m}$  thick Czochralski silicon sensors. As can be

seen from the figure, the base capacitance of these two sensors is different. This is due to the different thicknesses of the devices.

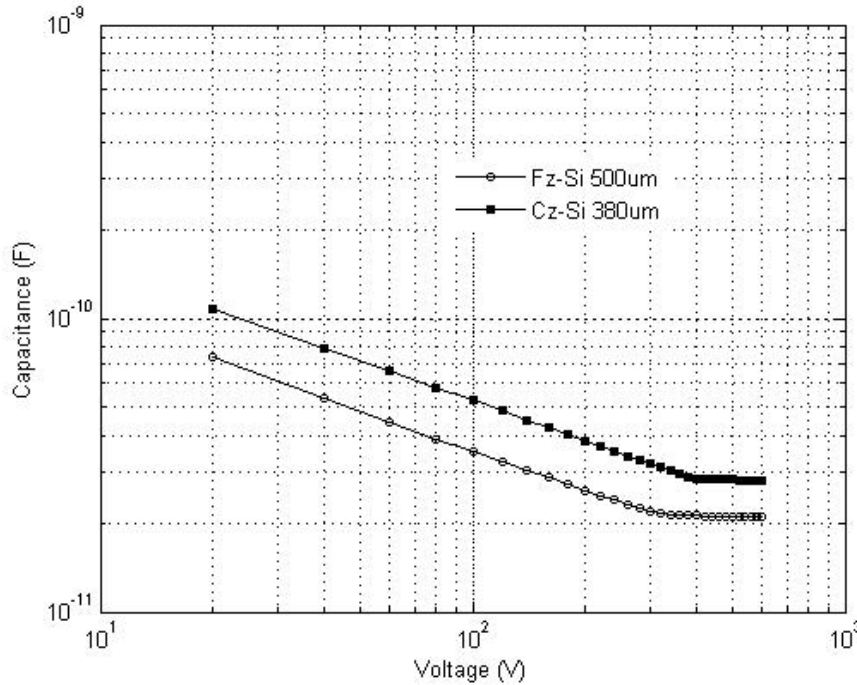


Figure 12. Double logarithmic capacitance-voltage graphs measured from a 500  $\mu\text{m}$  thick Float Zone silicon and a 380  $\mu\text{m}$  thick Czochralski silicon sensors.

### 3.3.2 TCT measurement

The Transient Current Technique method for detector characterization was developed by Ioffe Institute (St. Petersburg, Russia) and Brookhaven National Laboratory (Brookhaven, USA) [7] [41] [42] [43]. Using the TCT measurement it is possible to determine the full depletion voltage, effective trapping time and the sign of the space charge in the bulk. The TCT measurement is based on the detection of the dominant type of charge carrier, electron or hole, which drifts across the whole detector thickness after being triggered by a photon. This is achieved by illuminating the front ( $p^+$  implant) or back ( $n^+$  implant) side of the detector with a 660 nm diode laser, whose light penetrates a few microns into the silicon. The absorbed photons create electron-hole pairs close to the device surface (see Figure 13).

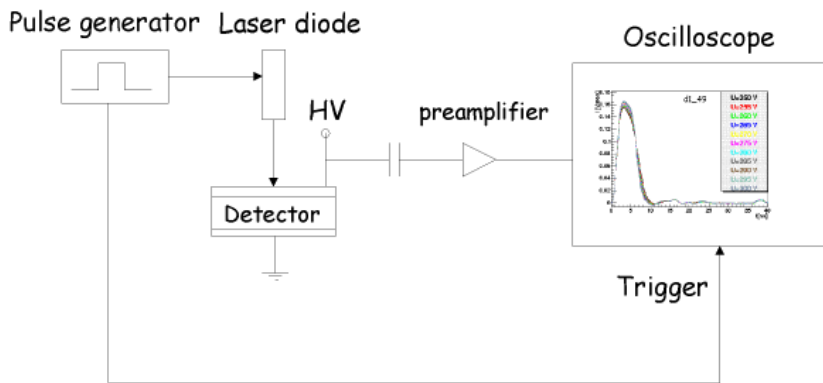


Figure 13. Schematic layout of a TCT measurement setup.

If the front side of the device is illuminated ( $p^+$  contact), the gathered current is coming from the electrons, and if the back side is illuminated, the hole current is measured. This is due to the fact that when the front side of the detector is illuminated, the holes are gathered to the  $p^+$ -electrode so fast that the signal is damped by the rise-time of the data acquisition (DAQ) electronics: the measured signal is therefore mainly coming from the electrons that travel a longer distance through the silicon bulk (Figure 14a and Figure 15). Correspondingly, when the back side of the detector is illuminated, mainly the hole current is measured, because the electrons are gathered rapidly on their closest electrode on the back side (Figure 14b and Figure 16).

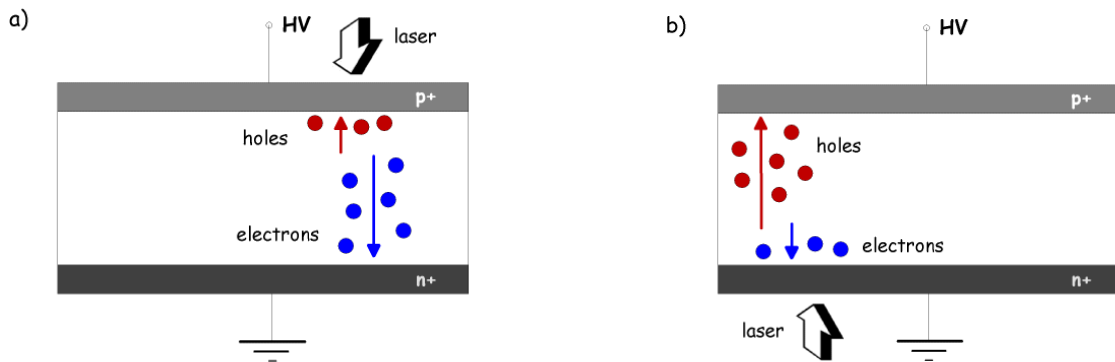


Figure 14. Transient Current Technique: a) electron dominated signal when the detector front side is illuminated and b) hole dominated signal when the detector backside is illuminated.

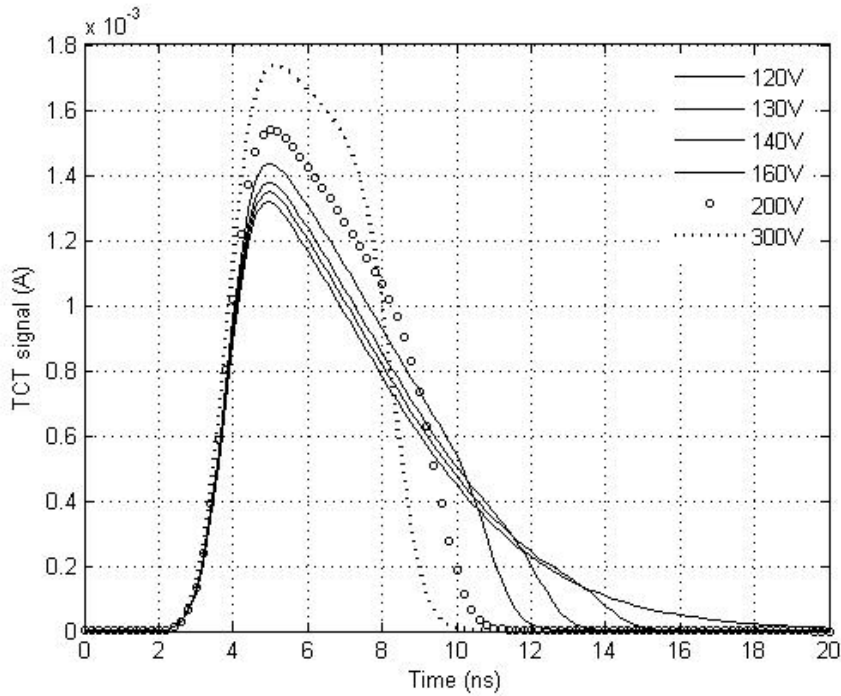


Figure 15. Current transients of the electron dominated signal, when the detector is illuminated from the front side. The curve with open symbols ( $\circ$ ) corresponds roughly to the  $V_{fd}$ . The curves with solid lines are with a voltage under the full depletion voltage and the curve with the dashed line is measured with a voltage above the full depletion. (Data V. Eremin)

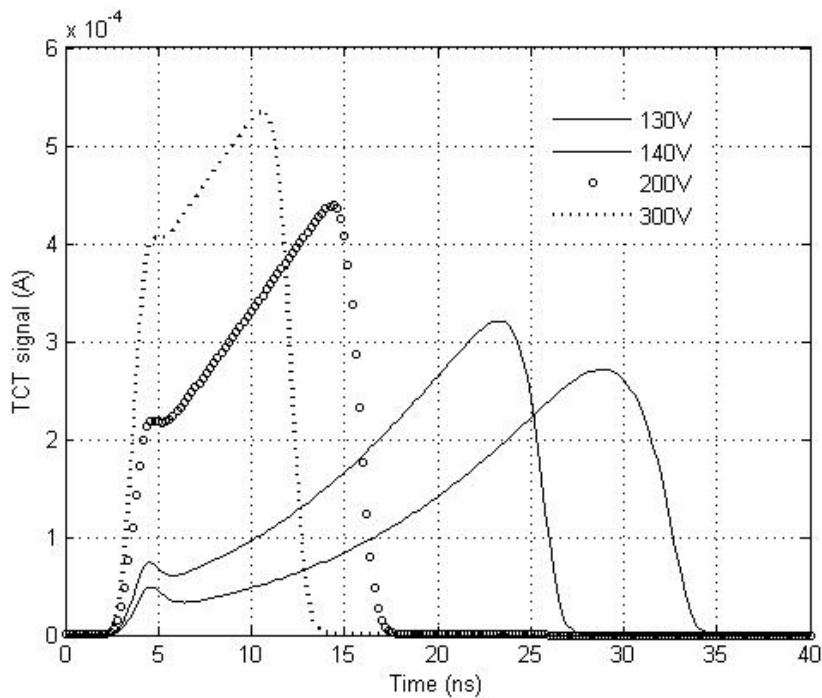


Figure 16. Current transients of the hole dominated signal, when the detector is illuminated from the back side. The curve with open symbols ( $\circ$ ) corresponds roughly to the  $V_{fd}$ . The curves with solid lines are with a voltage under the full depletion voltage and the curve with the dashed line is measured with a voltage above the full depletion. (Data V. Eremin)

Depending on the conductivity type of the bulk, the electric field, i.e. the collecting junction, is either on the front side or the back side of the detector. When measured from the front side, if the junction is on the front side, a descending electron transient current is measured. If the junction is on the back side, i.e. the bulk has inverted, an ascending electron transient current is measured. Similarly, when measured from the back side, an ascending hole transient current is measured if the junction is on the front side. If the bulk has inverted, the holes drift to the junction on the back side and then a descending hole transient current is seen.

### 3.3.3 DLTS measurement

Deep Level Transient Spectroscopy (DLTS) is an important technique for studying deep-level impurities and defects in semiconductors. It provides information about the position of the levels with respect to the corresponding band edge, their capture cross-section and their concentration in the crystal [44].

The DLTS is based on measuring the capacitance transient as a function of temperature. In the resulting DLTS spectrum, each level exhibits a peak whose height is proportional to the trap density, whose sign allows distinguishing between minority and majority traps and whose position on the temperature axis is determined by the activation energy and the cross-section.

The measurement is conducted by monitoring the capacitance transient by pulsing repetitively the p-n-junction from reverse bias to the ground potential. During the zero bias condition, the traps are filled with electrons. When the reverse bias is restored, the electrons are emitted into the conduction band as a function of time with corresponding transient capacitance:

$$C = C_0 \left[ 1 - \frac{n_T(0)}{2N_D} \exp\left(-\frac{t}{\tau_e}\right) \right] \quad (17)$$

with  $\tau_e$  depending on the temperature as:

$$\tau_e = \frac{1}{\gamma_n \sigma_n T^2} \exp\left(\frac{E_C - E_T}{kT}\right). \quad (18)$$

As can be seen from the equation, the time constant  $\tau_e$  increases with decreasing temperature.  $\gamma_n$  is a material coefficient depending on the material type and  $\sigma_T$  the capture cross-section. [45]

In the DLTS measurement, the so-called rate window concept is an essential part. Its key idea is that, from among several capacitance transient measurements, one capacitance decay rate is chosen to correspond to a maximum output signal. When a series of the

capacitance transient measurements is taken as a function of temperature, a peak appears at the  $C$ - $t$  versus temperature plot at the temperature that corresponds to the rate window capacitance decay rate. That is, if the  $C$ - $t$  waveforms are sampled at times  $t=t_1$  and  $t=t_2$  and the capacitance  $C(t_2)$  is subtracted from the capacitance  $C(t_1)$ , there is no difference between the capacitance at the two sampling times for very slow or very fast transients corresponding to low and high temperatures. A difference signal is generated when the time constant is in the order of  $t_2-t_1$  and the capacitance difference passes through a maximum as a function of temperature (see Figure 17). An example of DLTS peaks generated by radiation and process-induced traps is presented in Figure 18.

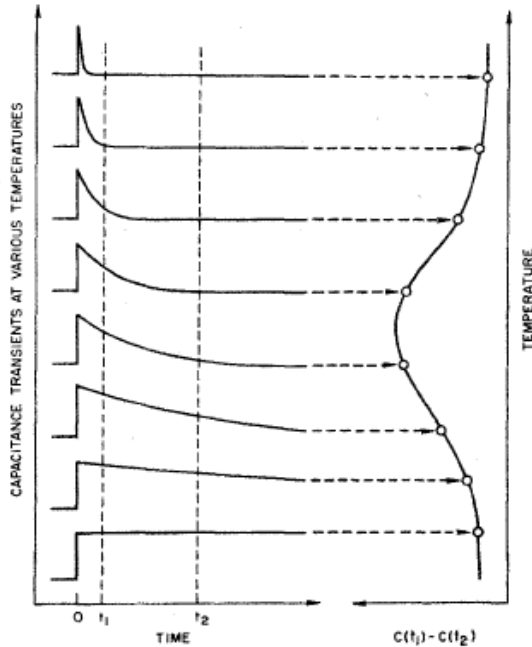


**Figure 17. Illustration of how the rate window is determined. The left-hand side shows capacitance transients at various temperatures, while the right-hand shows the corresponding DLTS signal resulting from using the double boxcar to display the difference between the capacitance at time  $t_1$  and the capacitance at time  $t_2$  as a function of temperature [46].**

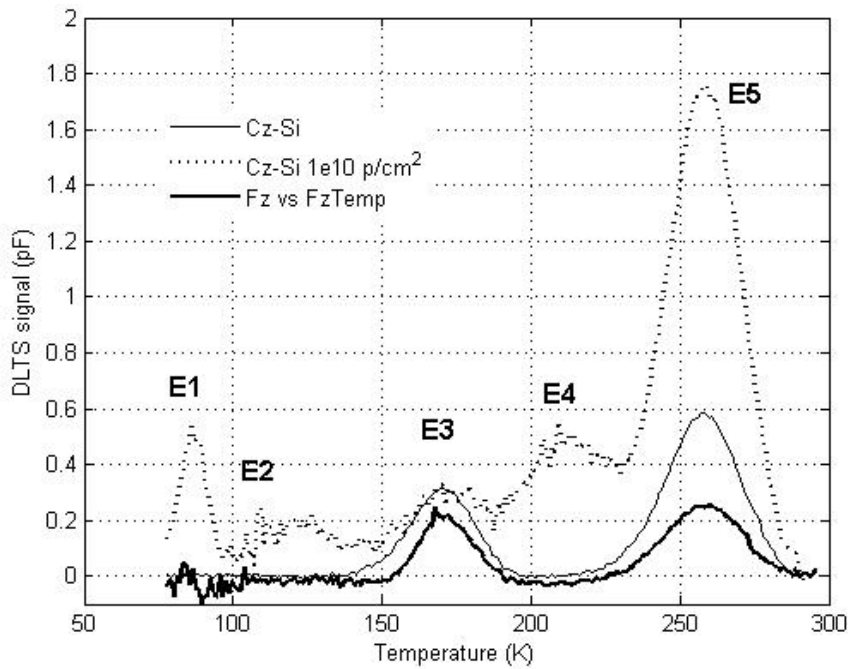


**Figure 18.** The DLTS spectra of non-irradiated FZ silicon and CZ silicon diodes and a proton-irradiated CZ silicon diode. The electron traps E1, E2 and E4 are radiation induced defects and traps E3 and E5 defects generated during the processing phase.

### 3.3.4 Beam telescope tests

Some important detector parameters such as efficiency, signal-to-noise (SNR) ratio and resolution of the large-area detectors were measured with the Silicon Beam Telescope [47] (SiBT) at CERN H2 experimental area using 225 GeV muons. The SiBT determined the tracks of the incoming particles, i.e. it provided the reference measurement for the detector characterization.

In the basic configuration, the SiBT consists of eight single-sided DC-coupled 1024-strip FZ detectors with a strip pitch of 55  $\mu\text{m}$  and the strip width of 14  $\mu\text{m}$  resulting in a total sensitive area of 5.6 x 5.6  $\text{cm}^2$ . Each detector is bonded to a hybrid containing eight 128-channel VA1 readout chips (Ideas ASA, Norway) [48] (see Figure 19) and has a separate repeater card.



**Figure 19. MCZ detector bonded to a SiBT readout hybrid.**

The repeater card contains four voltage regulators to supply the readout chips and a high-speed differential I/O amplifier to buffer and amplify the balanced analog output signal. Line receivers and analog and digital circuits control the readout electronics and set the necessary working parameters for the detector and the readout chips. In addition, the repeater card protects the readout chips against breakdown damage in the latch-up conditions. The detectors are installed as pairs orthogonal to the beam axis. Each pair consists of one detector with strips positioned vertically and one with strips positioned horizontally. During the beam test, the detectors under test replace one of the middle planes in the telescope.

The system trigger is provided by two standard plastic scintillators attached to photomultiplier tubes mounted before the first, and after the last, detector along the beam. The readout of the detectors is realized with a commercially available 8-channel VME ADC module (SIS3300, Struck Innovative Systeme GmbH, Germany) [49] and a PC Linux based Data Acquisition System (DAQ) realized with C++-code using object-oriented techniques [50]. The schematics of the SiBT layout are presented in Figure 20.

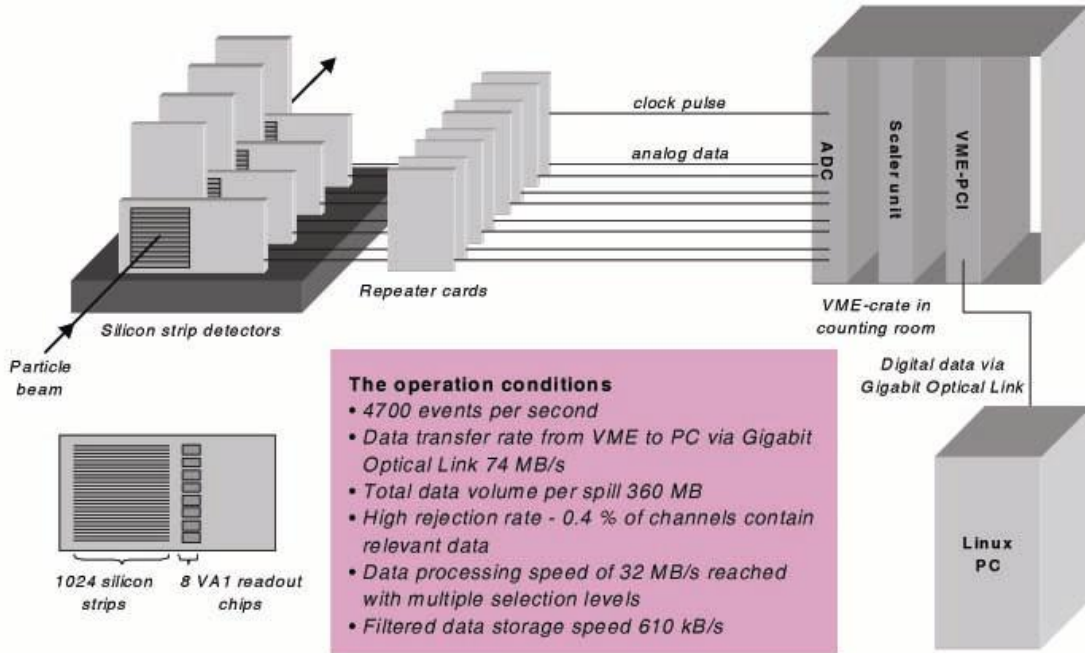


Figure 20. Schematics of the Silicon Beam Telescope (picture: L. A. Wendland).

The trigger signal starts the data readout sequence simultaneously on all of the detector repeater cards. The VME ADC module SIS3300 digitizes the analogue signals coming from the detectors and a VME-PCI interface transmits the data via an optical fiber to the PC, where the data are processed by the online monitoring program.

Since approximately 99.6 % of the raw data is only noise, the data have to be filtered and only the cluster information on each detector is saved, i.e. the position, the signal ( $S$ ), the noise ( $N$ ) and the pedestal ( $P$ ) for every strip participating in the cluster. In the online software, the  $P$  is defined for each strip as a long-term average of the raw data pulse ( $R$ ). The noise is defined as the standard deviation of  $R$ . Since the noise level stays sufficiently stable on the strips that are not dead or very noisy,  $N$  is calculated between each particle spill. In the online clustering algorithm, the strip is declared as a central strip if it satisfies a central strip condition  $S > N \times \text{constant}$ . The constant is chosen experimentally for each detector according to its performance during the test. If the consecutive strip also satisfies this condition, it is added to the cluster and the process continues until the condition is no longer satisfied. Then one strip adjacent to the cluster on each side of it is added to the cluster. However, if a noisy or a dead strip is part of the cluster, the cluster is discarded. In addition, only clusters with 10 strips or fewer are saved.

In the offline analysis, the cluster candidate is built from the saved cluster information and there is further filtering to the data, e.g. the cluster size cut, rejecting clusters with too many strips. Next, the exact position of the hit that corresponds to the cluster is calculated by applying the  $\eta$ -algorithm [51] to the pair of adjacent strips with the largest sum of charge. Then the local coordinates of the reconstructed hit positions in the telescope reference planes are transformed to the coordinates in the two projections ( $x$ - $z$  and  $y$ - $z$ , where  $z$  is the beam direction) of the system. Pattern recognition is used to find the particle tracks, i.e. coordinates along straight lines in the two projections are searched.

The track reconstruction is carried out as a sum-of-least-squares fit in three dimensions: a hit from all reference planes is required. The track candidates are accepted by the  $\chi^2$  criteria,

$$\chi^2 = \sum_{i=1}^d \frac{(x_{\text{impact},i} - x_{\text{hit},i})^2}{\sigma_i^2}, \quad (19)$$

where  $d$  is the number of the reference planes,  $x_{\text{impact},i} - x_{\text{hit},i}$  the residual of the reference plane  $i$ , i.e. the difference between the detector cluster center and the track, and  $\sigma_i$  the estimated detector resolution. If the calculated  $\chi^2$  is less than the set threshold (for example  $\chi^2 < 10$ ), the track is accepted.

To be able to measure the properties of the device under test, the system has to be aligned. The reference detectors are aligned manually with the reconstructed tracks. The first and the last pair of the detectors are kept fixed, while the others are moved in the direction perpendicular to the strips and rotated around the axis normal to their surface. The required translational corrections are determined from the mean values of the residual plots and the alignment is continued until the mean values of the residuals are close to zero. The rotational corrections are determined from the plots, where the residuals are plotted as a function of the coordinate along the strips. The angular corrections are continued until there is no correlation between the y-coordinate and the residual.

To calculate the properties of the detector under test, the tracks are interpolated to its front surface and the clusters near the track are identified. Then it is aligned with respect to the telescope.

The resolution of the device under test  $\sigma_{\text{dut}}$  is defined as:

$$\sigma_{\text{dut}} = \sqrt{\sigma_{\text{res,dut}}^2 - \sigma_{\text{ip,dut}}^2}, \quad (20)$$

where  $\sigma_{\text{res,dut}}$  is the standard deviation of the residuals  $x_{\text{impact,dut}} - x_{\text{hit,dut}}$  and the  $\sigma_{\text{ip,dut}}$  the impact point uncertainty. The detection efficiency is calculated by dividing the number of tracks for which a cluster with a residual smaller than  $\pm 2 \sigma_{\text{dut}}$  is observed by the total number of tracks. The signal-to-noise ratio (SNR) is calculated from the clusters with residuals smaller than the  $\pm 2 \sigma_{\text{dut}}$  by summing the signal from all the strips in the cluster and dividing it by the quadratic average noise of these strips.

## 4. Results and discussion

The results presented in the article I show that in the beam test, the non-irradiated large-area CZ silicon detector had a signal-to-noise ratio (SNR) of 10, a particle detection efficiency of 95% and a resolution of 10  $\mu\text{m}$ . Prior to the beam test, the electrical properties of the detector were also found to be appropriate: the detector was depleted with a reasonable operating voltage (420 V) with a leakage current of 2.4  $\mu\text{A}$ . This performance is comparable with that of devices made from standard materials such as standard or oxygenated FZ silicon.

The beam test results of the proton irradiated CZ silicon detector presented in the article IV indicate that the main criteria for a particle detector was fulfilled: the CZ silicon detector was able to detect particles even after the dose of  $1.6 \times 10^{14}$  1 MeV neutron  $\text{cm}^{-2}$  equivalent fluence with a SNR of 3, a spatial resolution of 20  $\mu\text{m}$  and an average particle detection efficiency of 36%. Naturally, these results are not sufficient for real particle tracking applications. However, it is likely that the bad performance of the detector was partly due to the generally high noise observed in the reference telescope, since also the FZ silicon reference detector with the same design had a SNR of only 7.5. Furthermore, the shaping time of the readout chip used in the beam test was considerably longer than in modern readout chips. The shaping time is known to affect the shot noise [53] [54]. This can be critical, especially in the case of irradiated detectors where the reverse current shot noise is much higher than in non-irradiated detectors. In addition, there might have been a large bias in the cluster selection, since all the clusters that contained a noisy or dead strip were rejected, as well as the clusters that had an SNR close to the pre-defined cut level.

The experimental results from the test diodes (presented in the articles I-VI) processed on the CZ silicon material show that the CZ silicon devices, when irradiated with low energy protons, are much less prone to the increase in the negative space charge than the standard or oxygenated FZ devices. In addition, the space charge sign inversion (SCSI) happens somewhere between the fluencies of  $1.6 \times 10^{14}$  and  $2.6 \times 10^{14}$  1 MeV neutron  $\text{cm}^{-2}$  equivalent fluence, and even after the dose of  $5 \times 10^{14}$  1 MeV neutrons  $\text{cm}^{-2}$  equivalent fluence, the depletion voltage of the CZ silicon devices is smaller than the pre-irradiation value. For comparison, a total dose of  $1.6 \times 10^{14}$  1 MeV neutron  $\text{cm}^{-2}$  equivalent fluence is predicted for the inner parts of the CMS Tracker after ten years of operation.

Besides, the leakage current of the CZ silicon devices does not seem to increase linearly as a function of the irradiation dose. This can be very beneficial for the power consumption in the large tracking detectors. However, when the CZ silicon devices are irradiated with high-energy protons, their behavior approaches that of DOFZ silicon devices. On the other hand, in the case of gamma irradiation, a positive space charge is induced into CZ silicon material and this introduction rate is even higher than in the DOFZ silicon, which is expected to be due to the irradiation induced reactivation of thermal donors. But no space charge sign inversion takes place in CZ silicon.

In the case of neutron irradiation, the CZ silicon material does not show any significant improvement compared to other silicon materials. However, the introduction rate of deep acceptors seems to be slightly lower in CZ silicon diodes than in FZ silicon diodes. Also, the SCSI happens similarly in both FZ and CZ silicon materials, and the threshold fluence scaled to 1 MeV neutron equivalent fluence is three times lower than in the case of low-energy protons.

Therefore, it can be concluded that, in the case of hadron irradiation, CZ silicon devices are more irradiation hard than the standard or oxygenated FZ devices. Additionally, in the case of other types of irradiation, CZ silicon devices behave similarly to the traditional detector materials.

However, one restriction of the presented characterization results arises from the fact that no test was run to see how the materials would be affected if same samples were irradiated with different types of irradiation. That would be much closer to the conditions in real experiment where it is possible that some of the effects cancel or enhance each other. In addition, some of the characterization methods used in this study might not be suitable for heavily irradiated samples since the electric field in such samples behaves differently than in the classical p-n-junction theory, i.e. so-called double junction is formed [55] [56]. Furthermore, the measured devices were designed and processed entirely by our research group and we might have unintentionally overlooked some matters affecting the results: for example, we did not make any surface passivation layer on our detectors, which in turn may have resulted in additional detector noise caused by eventual scratches on the surface.

On the grounds of diode measurements, it is interesting to think of the option where the detectors closest to the beam pipe in the CMS Tracker were made of Czochralski silicon. The innermost layers of the CMS tracking system consist of silicon pixel detectors delivering precise space point information with high resolution. The extremely high particle fluxes at the small distance from the collision point create a very hostile radiation environment. The present silicon pixel detectors are designed to survive up to  $6 \times 10^{14}$   $\text{cm}^{-2}$  1 MeV neutron equivalent fluence without an unacceptable degradation in their performance. This fluence corresponds roughly to the first four years from the LHC startup at the smallest radius.

At the full luminosity, the innermost pixel detectors are exposed to a fluence of  $3 \times 10^{14}$  1 MeV neutrons  $\text{cm}^{-2}$  per year. The fluence to the second and the third layer of detectors is about  $1.2 \times 10^{14}$  1 MeV neutrons  $\text{cm}^{-2}$  and  $0.6 \times 10^{14}$  1 MeV neutrons  $\text{cm}^{-2}$  per year, respectively [1]. This implies that some parts of the pixel detector structure have to be replaced during the lifetime of the CMS experiment. The sensor lifetime is mainly limited by the insufficient charge collection caused by trapping and incomplete depletion. Both can be compensated by increasing bias voltage, which can eventually lead to an electrical breakdown. If these pixel detectors were processed from CZ silicon, on the light of our results they would stand much higher operational voltages.

In addition, since the full depletion voltage of CZ silicon devices is still smaller than the pre-irradiation value even after the dose of  $5 \times 10^{14}$  1 MeV neutrons  $\text{cm}^{-2}$  equivalent fluence, it would take much longer to reach the non-tolerable voltages than in the case of present devices. Additionally, since in CZ silicon material the leakage current does not seem to increase linearly as a function of the irradiation dose, the noise profile of the detector might not change as radically, which in turn is beneficial for the particle detection efficiency [57]. Therefore, the innermost detectors might not need a replacement during the CMS operation and the detectors farther away from the beam pipe might even be able to stand the possible LHC luminosity upgrade with an acceptable deterioration in their performance.

## 5. Conclusions

The purpose of this work was to prove by different characterization methods that magnetic Czochralski silicon material is suitable for particle detection applications. The properties of MCZ silicon devices were characterized by several different methods: current-voltage and capacitance-voltage measurement techniques, transient current technique, deep-level transient spectroscopy and a reference beam telescope. Pad detectors were irradiated to various fluencies with low- and high-energy protons, neutrons and  $^{60}\text{Co}$  gamma rays. The devices were characterized before and after irradiation. In addition, large-area ( $32.5\text{ cm}^2$ ) strip detectors were characterized in particle beam before and after irradiation to  $1.6 \times 10^{14}\text{ cm}^{-2}$  1 MeV neutron equivalent fluence.

The results presented in the articles (I-IV) clearly encourage further investigations concerning the magnetic Czochralski silicon material. It is potentially irradiation hard, especially in the case of charged hadrons and thus a promising material for tracking applications in future high-energy physics experiments. In addition, from this material it is possible to manufacture large detectors with a relatively simple manufacturing process. However, it needs to be remembered that in CZ silicon thermal donors are formed at certain temperatures, which decreases the effective bulk resistivity. Nevertheless, with correct processing the TD formation can be effectively suppressed. Furthermore, it has been shown that the MCZ detector irradiated to a  $1.6 \times 10^{14}\text{ cm}^{-2}$  1 MeV neutron equivalent fluence still detects particles. Although the beam test results are relatively modest, the MCZ silicon is definitely worth of further investigations as detector material. In addition, on the basis of these results we would suggest that in the future beam tests should be conducted with modern readout chips such as APV25 [58].

## References

- [1] *CMS Tracker Technical Design Report 5*, CERN/LHCC 98-6 (1998).
- [2] *ATLAS Inner Detector Technical Design Report 5*, CERN/LHCC 97-17 (1997).
- [3] P. W. Higgs, *Broken symmetries, massless particles and gauge fields*, Physics Letters 12 (1964) 132-133.
- [4] P. W. Higgs, *Spontaneous Symmetry Breakdown without Massless Bosons*, Physical Review 145 (1966) 1156-1163.
- [5] G. Lindström, *Radiation damage in silicon detectors*, Nuclear Instruments and Methods in Physics Research A 512 (2003) 30-43.
- [6] E. Fretwurst et al., *Recent advancements in the development of radiation hard semiconductor detectors for S-LHC*, Nuclear Instruments and Methods in Physics Research A 552 (2005) 7-19.
- [7] Z. Li et al., *Investigation of the Oxygen-Vacancy (A-Center) Defect Complex Profile in Neutron Irradiated High Resistivity Silicon Junction Particle Detectors*, IEEE Transactions on Nuclear Science 39 (6) (1992) 1730-1738.
- [8] Z. Li et al., *Elevated Temperature Annealing of the Neutron Induced Reverse Current and Corresponding Defect Levels in Low and High Resistivity Silicon Detectors*, IEEE Transactions on Nuclear Science 42 (4) (1995) 387-393.
- [9] G. Lindström et al., *Radiation hard silicon detectors-developments by the RD48 (ROSE) collaboration*, Nuclear Instruments and Methods in Physics Research A 466 (2001) 308-326.
- [10] A. Ruzin, *Comparison of Radiation Damage in Silicon Induced by Proton and Neutron Irradiation*, IEEE Transactions on Nuclear Science 46 (5) (1999) 1310-1313.
- [11] L. Fonseca et al., *Silicon wafer oxygenation from SiO<sub>2</sub> layers for radiation hard detectors*, Microelectronics Reliability 40 (2000) 791-794.
- [12] W. Zulehner, *Czochralski growth of silicon*, Journal of Crystal Growth 65 (1983) 189-213.
- [13] R. W. Series and D. T. J. Hurle, *The use of magnetic fields in semiconductor crystal growth*, Journal of Crystal Growth 113 (1991) 305-328.
- [14] D. T. J. Hurle and E. Jakeman, *Natural Oscillations in heated fluid layers*, Physics Letters 43A (1973).
- [15] S. M. Sze, *Physics of Semiconductor Devices*, 2<sup>nd</sup> edition, John Wiley & Sons (1981).
- [16] S. M. Sze, *Semiconductor Devices, Physics and Technology*, 2<sup>nd</sup> edition, John Wiley & Sons (2001).
- [17] R. C. Alig and S. Bloom, *Electron-hole pair creation energies in semiconductors*, Physical Review Letters 35 22 (1975) 1522-1525.
- [18] M. Laakso, P. Singh and P.F. Shepard, *Field oxide radiation damage measurements in silicon strip detectors*, Nuclear Instruments and Methods in Physics Research A 327 (1993) 517-522.
- [19] S. Eidelman et al., *Review of Particle Physics*, Physics Letters B 592 1 (2004).
- [20] A. Vasilescu and G. Lindström, *Notes on the fluence normalization based on the NIEL scaling hypothesis*, ROSE/TN/2002-02 (2000).

- [21] A. Vasilescu and G. Lindstroem, *Displacement Damage in Silicon*, Online compilation, [referred 15.7.2005], <http://sesam.desy.de/members/gunnar/Si-dfuncs.html>.
- [22] M. Huhtinen, *Simulation of non-ionising energy loss and defect formation in silicon*, Nuclear Instruments and Methods in Physics Research A 491 (2002) 194-215.
- [23] G. Lindström et al., *Developments for radiation hard silicon detectors by defect engineering-results by the CERN RD48 (ROSE) Collaboration*, Nuclear Instruments and Methods in Physics Research A 465 (2001) 60-69.
- [24] S. Saramad, *A new explanation for some open questions of hadron irradiated silicon detectors*, Nuclear Instruments and Methods in Physics Research A 510 (2003) 101-106.
- [25] G. Hall, *Issues for deep level models of bulk damage to silicon detectors*, Nuclear Instruments and Methods in Physics Research A 388 (1997) 283-288.
- [26] C.S Fuller et al., *Resistivity changes in silicon single crystals induced by heat treatment*, Acta Metallurgica (1955) 97-99.
- [27] W. Kaiser, *Electrical and Optical Properties of Heat-Treated Silicon*, Physical Review 105 (1957) 1751- 1756.
- [28] W. Kaiser, H. L. Frisch and H. Reiss, *Mechanism of the formation of Donor States in Heat-Treated silicon*, Physical Review 112 (1958) 1546-1554.
- [29] D. Yang, D. Que and K. Sumino, *Nitrogen effects on thermal donor and shallow thermal donor in silicon*, Journal of Applied Physics 77 (1995) 943-944.
- [30] M. Moll, E. Fretwurst and G. Lindström, *Leakage current of hadron irradiated silicon detectors – material dependence*, Nuclear Instruments and Methods in Physics Research A 426 (1999) 87-93.
- [31] M. Moll, *Radiation Damage in Silicon Particle Detectors –microscopic defects and macroscopic properties*, Doctoral thesis, Universität Hamburg (1999).
- [32] G. Casse, *The effect of hadron irradiation on the electrical properties of particle detectors made from various silicon materials*, Thèse, Université Joseph Fourier-Grenoble 1 (1998).
- [33] S. Lazanu, I. Lazanu, *Annealing of radiation-induced defects in silicon in a simplified phonological model*, Nuclear Instruments and Methods in Physics Research B 183 (2001) 383-390.
- [34] D. Bechevet et al., *Results of irradiation tests on standard planar silicon detectors with 7-10 MeV protons*, Nuclear Instruments and Methods in Physics Research A 479 (2002) 487-497.
- [35] J. Härkönen et al., *Processing of microstrip detectors on Czochralski grown high resistivity silicon substrates*, Nuclear Instruments and Methods in Physics Research A 514 (2003) 173-179.
- [36] M. Bruzzi et al., *Thermal donor generation in Czochralski silicon particle detectors*, Nuclear Instruments and Methods in Physics Research A, article in press.
- [37] A. Virtanen et al, *Heavy ion and proton test site at JYFL-accelerator laboratory*, Nuclear Instruments and Methods in Physics Research A 426 (1999) 68-71.
- [38] M. Glaser et al, *New irradiation zones at the CERN-PS*, Nuclear Instruments and Methods in Physics Research A 426 (1999) 72-77.

- [39] Gunter H.R. Kegel, David DeSimone, *Facilities for gamma and neutron irradiations*, Nuclear Instruments and Methods in Physics Research A 426 (1999) 61-67.
- [40] Instrumentation Division, *The Solid State Gamma-ray Irradiation Facility*, [referred 20.6.2005], <<http://www.inst.bnl.gov/SSIF/Overview.html>>.
- [41] V. Eremin and Z. Li, *Determination of the Fermi-level position for neutron irradiated high resistivity silicon detectors and materials using the transient charge technique (TChT)*, IEEE Transactions on Nuclear Science 41 (6) (1994) 1907-1912.
- [42] V. Eremin, Z. Li and I. Iljashenko, *Trapping induced Neff and electrical field transformation at different temperatures in neutron irradiated high resistivity silicon detectors*, Nuclear Instruments and Methods in Physics Research A 360 (1995) 458-462.
- [43] V. Eremin et al., *Development of transient current and charge techniques for the measurement of effective net concentration of ionized charges (Neff) in the space charge region of p-n junction detectors*, Nuclear Instruments and Methods in Physics Research A 372 (1996) 388-398.
- [44] M. Henini, B. Tuck and C.J. Paull, *A microcomputer-based deep level transient spectroscopy (DLTS) system*, J. Phys. E. 18 (1985) 926-929.
- [45] D.K. Schroder, *Semiconductor Material and Device Characterization*, John Wiley & Sons, Inc. (1990).
- [46] D.V. Lang, *Deep-level transient spectroscopy: A new method to characterize traps in semiconductors*, Journal of Applied Physics 45 (1974) 3023-3032.
- [47] C. Eklund et al, *Silicon beam telescope for CMS detector tests*, Nuclear Instruments and Methods in Physics Research A 430 (1999) 321-332.
- [48] Ideas ASA, *VA Family*, [28.7.2005], <http://www.ideas.no/products/ASICs/VAFamily.html>.
- [49] Struck Innovative Systeme GmbH, *SIS3300 8 Channels 100 MHz 12-bit ADC*, [28.7.2005], <http://www.struck.de/sis3300.htm>.
- [50] L.A. Wendland et al, *Novel Data Acquisition System for Silicon Tracking Detectors*, CMS Conference Report CMS CR 2004/009 (2003).
- [51] E. Belau, *Charge collection in silicon strip detectors*, Nuclear Instruments and Methods 214 (1983) 253-260.
- [52] V. Karimäki, *Explicit Covariance Matrix for Particle Measurement Precision*, CMS NOTE-1997/064.
- [53] M. Meschini et al., *Performance of CMS silicon microstrip detectors with the APV6 readout chip*, Nuclear Instruments and Methods A 447 (2000) 133-141.
- [54] C. Bozzi, *Signal-to-Noise Evaluations for the CMS Silicon Microstrip Detectors*, CMS NOTE-1997/026.
- [55] V. Eremin et al., *Double peak electric field distortion in heavily irradiated silicon strip detectors*, Nuclear Instruments and Methods A 535 (2004) 622-631.
- [56] A. Castaldini, A. Cavallini and L. Polenta, *Double-junction effect in proton irradiated silicon diodes*, Journal of Applied Physics 92 (2002) 2013-2016.
- [57] J. Härkönen et al., *The effect of oxygenation on the radiation hardness of silicon studied by surface photovoltage method*, IEEE Transactions on Nuclear Science 49 (6) (2002) 2910-2913.

- [58] M.J. Frech et al., *Design and results from the APV25, a deep sub-micron CMOS front-end chip for the CMS Tracker*, Nuclear Instruments and Methods A 466 (2001) 359-365.

## List of Symbols

$qV_{bi}$	built-in potential.
$N_a$	acceptor atom density
$N_d$	donor density
$W$	depletion region thickness
$d$	detector thickness
$x$	distance
$\phi$	electric potential
$E$	electric field
$\rho$	space charge density
$\epsilon\epsilon_0$	permittivity of silicon
$q$	elementary charge
$N_{eff}$	effective doping concentration
$V$	reverse voltage
$V_{dep}$	depletion voltage
$C$	junction capacitance
$dQ$	incremental change in depletion layer charge
$dV$	incremental change in the applied voltage
$Q$	space charge
$A$	area of the device
$I_{bulk}$	bulk generation current
$\tau_g$	generation lifetime
$v_{th}$	thermal velocity
$N_t$	defect density
$\sigma_p$	hole capture cross-section
$\sigma_n$	electron capture cross-section
$E_t$	defect energy level
$E_i$	intrinsic energy level
$k_B$	Boltzmann's constant
$T$	absolute temperature
$n_i$	intrinsic carrier concentration of silicon
$N_c$	effective density of states in the conduction band
$N_v$	effective density of states in the valence band
$E_g$	band gap of silicon
$T_c$	comparison temperature
$T_m$	measurement temperature
$V_B$	breakdown voltage
$E_B$	breakdown electric field
$N_D$	donor doping density
$D$	displacement damage cross-section
$D_n$	displacement damage cross section for 1 MeV neutrons
$E$	kinetic energy
$\kappa$	hardness factor
$I_{leak}$	leakage current

$\tau_e$	time constant
$\gamma_n$	material coefficient depending on the material type
$\sigma_T$	capture cross-section
$t$	time
$S$	signal
$N$	noise
$P$	pedestal
$R$	raw data pulse
$x_{impact,i} - x_{hit,i}$	residual of the reference plane $i$
$\sigma_i$	estimated detector resolution
$\sigma_{dut}$	resolution of the device under test
$\sigma_{res,dut}$	standard deviation of the residuals $x_{impact,dut} - x_{hit,dut}$
$\sigma_{ip, dut}$	impact point uncertainty

## List of abbreviations

ADC	Analog-to digital converter
BHF	Buffered hydrogen fluoride
CCE	Charge collection efficiency
CMS	Compact Muon Solenoid
CV	Capacitance-voltage
CZ	Czochralski
DAQ	Data acquisition
DLTS	Deep level transient spectroscopy
DOFZ	Diffusion oxygenated Float Zone
EGS	Electronic grade polycrystalline silicon
FZ	Float Zone
FTIR	Fourier transform infrared
HEP	High-energy physics
HTLT	High-temperature long-time
I/O	Input/Output
IV	Current-voltage
LHC	Large Hadron Collider
MCZ	Magnetic Czochralski
MEC	Microelectronics Centre of Helsinki University of Technology
MIP	Minimum ionizing particle
NIEL	Non-ionizing energy loss
PCI	Peripheral component interconnect
PKA	Primary knock-on atom
RCA	Radio Corporation of America
RF	Radio-frequency
RH	Radiation hardness
SCSI	Space charge sign inversion
SiBT	Silicon Beam Telescope
SNR	Signal to noise ratio
TCT	Transient current technique
TD	Thermal donor
TSC	Thermally stimulated current
VME	VERSA-Module Europe
VO	Vacancy-oxygen